

**1 Analysis of the 1 December 2011 Wasatch downslope windstorm**

**2 JOHN LAWSON \* AND JOHN HOREL**

*Department of Atmospheric Science, University of Utah, Salt Lake City, Utah, United States of America.*

---

\* Corresponding author address: John Lawson, Department of Geological and Atmospheric Science, Iowa State University, Ames, IA 50011.

E-mail: john.rob.lawson@googlemail.com

## ABSTRACT

4 A downslope windstorm on 1 December 2011 led to considerable damage along a narrow 50-  
5 km swath at the western base of the Wasatch Mountains in northern Utah. The strongest  
6 surface winds began suddenly at 0900 UTC, primarily in the southern portion of the damage  
7 zone. Surface winds reached their peak intensity with gusts to  $45 \text{ m s}^{-1}$  at  $\sim 1600 \text{ UTC}$ , while  
8 the strongest winds shifted later to the northern end of the damage swath. The northward  
9 shift in strong surface winds relates to the rotation of synoptic-scale flow from northeasterly  
10 to easterly at crest level, controlled by an evolving anticyclonic Rossby-wave-breaking event.  
11 A rawinsonde released at  $\sim 1100 \text{ UTC}$  in the midst of strong ( $>35 \text{ m s}^{-1}$ ) easterly surface  
12 wind intersected a rotor and sampled the strong inversion that surmounted it.

13 The windstorm's evolution was examined further via Weather Research and Forecasting  
14 model simulations initialized from North American Mesoscale analyses  $\sim 54 \text{ h}$  before the  
15 windstorm onset. The control model simulation captured core features of the event, including  
16 the spatial extent and timing of the strongest surface winds. However, the model developed  
17 stronger mountain-wave breaking in the lee of the Wasatch, a broader zone of strong surface  
18 winds, and a downstream rotor located farther west than observed. A second simulation, in  
19 which the nearby east–west-oriented Uinta mountains were reduced in elevation, developed  
20 weaker easterly flow across the Wasatch during the early stages of the event. This result  
21 suggests that the Uinta Mountains block and steer the initial northeasterly flow across the  
22 Wasatch.

## <sup>23</sup> 1. Introduction

<sup>24</sup> Downslope windstorms arise when a layer of air is sandwiched between a terrain bar-  
<sup>25</sup> rier and a strongly-stable layer aloft, while being forced over the barrier (Markowski and  
<sup>26</sup> Richardson 2010). Due to the damage often associated with downslope windstorms, they  
<sup>27</sup> have obtained local names in areas experiencing them frequently, including the föhn, bora,  
<sup>28</sup> chinook, zonda, Santa Ana, Wasatch, and Washoe Zephyr (Whiteman 2000; Richner and  
<sup>29</sup> Hächler 2013). As discussed by Richner and Hächler (2013), the general synoptic features  
<sup>30</sup> associated with localized downslope windstorms are well understood and reasonably well  
<sup>31</sup> predicted.

<sup>32</sup> The Wasatch windstorm of 1 December 2011 caused over \$75 million damage in a narrow  
<sup>33</sup> swath, roughly 3–5 km wide and 50 km long as delineated by the hatched rectangular box  
<sup>34</sup> in Fig. 1a along the Wasatch Front (O'Donoghue 2012). The Wasatch Front describes the  
<sup>35</sup> urban–suburban corridor paralleling the west slopes of the Wasatch Mountains. Impacts of  
<sup>36</sup> this storm, which was later declared a federal disaster, included: as many as 70,000 trees  
<sup>37</sup> were uprooted or damaged; power was lost in many communities after over 22 transformers  
<sup>38</sup> were damaged and 1.5 km of power lines required maintenance; rail traffic was halted along  
<sup>39</sup> the Wasatch Front; and Interstate 15 was closed to large vehicles after many were blown  
<sup>40</sup> over on the freeway.

<sup>41</sup> An anemometer sited by Union Pacific Railroad in Centerville, UT (UP028 in Fig. 1b),  
<sup>42</sup> along a stretch of rail line prone to high winds during downslope windstorms, recorded a  
<sup>43</sup> maximum gust of  $45 \text{ m s}^{-1}$  (102 mph) at  $\sim 1600 \text{ UTC}$ <sup>1</sup> 1 December 2011 (Fig. 2). Strong  
<sup>44</sup> winds were not only observed along the Wasatch Front on this day, but also in other localized  
<sup>45</sup> areas across the western United States; for example, southern California experienced one of  
<sup>46</sup> its strongest Santa Ana events in recent years (Welch and Rice 2011).

<sup>47</sup> Forecasting the occurrence of downslope windstorms has long been recognized to re-  
<sup>48</sup> quire several critical ingredients (Smith 1985; Markowski and Richardson 2010). Follow-

---

<sup>1</sup>Local time in Utah is 7 h earlier than UTC during winter.

49 ing Markowski and Richardson (2010), the terrain barrier must first be: (1) quasi-two-  
50 dimensional so that air cannot simply flow around it, and (2) asymmetrical with a more  
51 gentle windward slope combined with a steep lee slope (Miller and Durran 1991). However,  
52 no single terrain characteristic is tied to strong-windstorm environments. Figure 2 depicts  
53 the steep lee-side profile along the Wasatch Front, near Centerville, UT. Here, the flat base  
54 of elevation 1280 m above mean sea-level rises eastward towards the crest of the Wasatch  
55 mountains (2500–2750 m in this region).

56 Second, a sufficiently-strong cross-barrier wind ( $>15 \text{ m s}^{-1}$ ) must impinge on the barrier;  
57 a wind direction orthogonal to a two-dimensional barrier will maximize the cross-product of  
58 the crest orientation and wind direction, and hence mountain wave excitation in the same  
59 direction downstream. Third, the vertical profiles of temperature, moisture, and wind should  
60 be conducive to amplifying the development of mountain lee waves. This typically requires  
61 one or more of the following characteristics: (1) a strongly-stable layer upstream of and  
62 above the crest level (Vosper 2004); (2) an environmental critical level above crest level,  
63 where the cross-wind component decreases to zero and/or reverses direction (e.g., Wang and  
64 Lin 1999); (3) a wave-induced critical level (Peltier and Clark 1979), where wave-breaking  
65 itself generates a wind reversal above crest level that is not found in upstream wind profiles;  
66 or (4) the synoptic environment should favor subsidence aloft, but not favor the development  
67 of a deep cold-air pool in the lee of the range that might inhibit penetration of strong winds  
68 to the surface (Jiang and Doyle 2008).

69 National Weather Service (NWS) forecasts issued by the Salt Lake City Forecast Office  
70 for the 1 December 2011 Wasatch windstorm were ample for public and private contingency  
71 planning in terms of spatial and temporal accuracy, forecast lead time, and wind speed  
72 magnitude. The first Area Forecast Discussion (AFD) to mention a potential for strong  
73 winds along the Wasatch Front on 1 December was issued at 1712 UTC 27 November (90 h  
74 before the onset of the windstorm) and the matter was discussed in the subsequent Hazardous  
75 Weather Outlook (HWO). All further AFDs and HWOs issued by the Salt Lake City Forecast

76 Office mentioned the chance for high winds, with increasing confidence as the event drew  
77 closer. The potential for high winds was cited in many AFDs to be based on: (1) the  
78 similarity between the developing synoptic situation and situations observed during prior  
79 major Wasatch windstorms, and (2) confidence in both the numerical model guidance from  
80 operational forecast models and a higher-resolution model run locally at the Forecast Office  
81 <sup>2</sup>.

82 Planning for this study began the day before the windstorm, and was motivated by  
83 a number of factors: (1) operational numerical guidance and forecaster experience led to  
84 high confidence that a major downslope windstorm was possible; (2) verification of this  
85 forecast would lead to the first major downslope windstorm along the Wasatch Front in over  
86 a decade; (3) experimental high-resolution numerical forecasts run by the Salt Lake City  
87 National Weather Service Office were providing considerable specificity regarding the details  
88 of the impending windstorm; and (4) routine automated observations were already in place  
89 throughout the region such that additional observational assets available in the Department  
90 of Atmospheric Sciences could be used advantageously to mount a small field campaign to  
91 study the event (the equipment available has been described by Lareau et al. 2013). On  
92 30 November, a University of Utah (UoU) team quickly drew up a research plan to collect  
93 additional observations the next day using surface weather stations, portable rawinsonde  
94 systems, and vehicle-mounted sensors. While a major downslope windstorm was deemed  
95 likely by forecasters, and supported by high-resolution deterministic model output, UoU  
96 team confidence was not particularly high regarding the specific details (timing, location,  
97 and intensity) of the high-resolution numerical guidance provided by the NWS.

98 The resulting severity of the event, combined with the accuracy of the high-resolution

---

<sup>2</sup>Weather Research and Forecasting mesoscale model runs were made four times a day with boundary conditions based on the prior Global Forecast System model. The regional domain was 12 km, and nested down to 4 km across Utah. Each run produced hourly guidance through 60 forecast hours. This was the first major Wasatch windstorm where forecasters had access to high-resolution forecast guidance in their operational office environment (Randy Graham and Steve Rogowski, 2012, personal communication).

model guidance, the apparent extended predictability, and an unprecedented data set for a Wasatch downslope windstorm, ultimately led to completion of this study. Our objectives are to examine the 1 December 2011 Wasatch downslope windstorm from several distinct perspectives: (1) relate briefly this event to previous downslope windstorms; (2) analyze the spatial and temporal evolution of the winds on the basis of local observations from conventional sources and those collected specifically during the small field campaign; (3) evaluate a high-resolution model simulation in terms of its ability to resolve the mesoscale and local features of the event; and (4) assess the impacts of the upstream Uinta Mountains that may deflect the flow traveling towards the Wasatch Mountains. Lawson (2013) provides additional details about this research.

## 2. Data and Model Configuration

### a. Observational data

Surface observations of meteorological and other environmental parameters were obtained from the MesoWest archive (Horel et al. 2002b). Reports from over 280 automated reporting stations were available within 80 km (50 mi) of Centerville, UT, the location of the strongest winds on 1 December 2011. There are substantive differences in the siting, equipment, and reporting characteristics of the automated observations available in MesoWest. Wind observations were manually evaluated to identify the time and intensity of the strongest observed winds.

An ad hoc UoU team of staff and students assembled during the morning of 30 November 2011 to determine where additional observations would help to document the expected windstorm. Decisions were made and implemented that afternoon to deploy three automated weather stations (locations shown in Fig. 1b): (1) near Morgan, UT (MesoWest identifier UFD06), immediately east of the Wasatch Range and located roughly along the cross section shown in Fig. 1a to monitor conditions upstream of the Wasatch; (2) east of Bountiful, UT

124 (UFD05), ~500 m in elevation above the foot of the slope and as far up as it was practical  
125 to drive given the weather and mountain road conditions; and (3) Farmington (UFD04) in  
126 Farmington, UT, ~1.5 km west of the base of the Wasatch. Two mobile Graw rawinsonde  
127 systems were prepared for the next day: one to be sited where the portable automated  
128 weather station was deployed near Morgan, UT (upstream of the Wasatch Range); the other  
129 to be deployed as needed in the lee of the range based on how the conditions evolved. Two  
130 vehicles were also equipped with roof-mounted GPS, wind, temperature, humidity, and pres-  
131 sure sensors. However, one of the roof-mounted racks was destroyed early the next day in  
132 the high winds.

133 *b. Model setup*

134 Numerical simulations were performed with the Weather Research and Forecasting (WRF)  
135 model, version 3.4, using the Advanced Research WRF dynamical core. All runs comprised  
136 three nested domains of grid size 12, 4, and 1.3 km (Fig. 3), whose initial and boundary  
137 conditions (updated every 6 h) were provided by North American Mesoscale (NAM) model  
138 analyses. The domains allowed two-way feedback; high-frequency waves were damped with  
139 sixth-order diffusion on the largest domain. Topography was interpolated from datasets at a  
140 resolution of 10 min for the 12-km domain, and 30 s for the 4- and 1.33-km domains, to the  
141 WRF-model grids. To avoid Courant-Friedrichs-Lowy criterion violation in regions of active  
142 mountain-wave breaking, vertical resolution was limited to 40 vertical levels. WRF out-  
143 put was interpolated onto a pressure-coordinate grid. Further details and parametrization  
144 options are listed in Table 1.

<sup>145</sup> **3. Results**

<sup>146</sup> *a. Climatology*

<sup>147</sup> Windstorms along the Wasatch Front (Fig. 1) occur in climatologically-anomalous east-  
<sup>148</sup> erly flow at crest level (Holland 2002; Horel et al. 2002a). Easterly windstorms (e.g., Mass  
<sup>149</sup> and Albright 1985; Jones et al. 2002) are hence rarer than those that occur on lee slopes  
<sup>150</sup> downwind of prevailing midlatitude westerly flows (e.g., Lilly and Zipser 1972; Zhong et al.  
<sup>151</sup> 2008). As discussed by Holland (2002), few meteorological surface stations in the vicinity  
<sup>152</sup> of the Wasatch Mountains are located in appropriate locations or have extensive enough  
<sup>153</sup> records to develop climatologies of Wasatch windstorms. For example, the Salt Lake Inter-  
<sup>154</sup> national Airport (KSLC in Fig. 1) is too far west of the range and does not experience strong  
<sup>155</sup> downslope winds during these events.

<sup>156</sup> Following Holland (2002), observations from Hill Air Force Base (KHIF, Layton, UT in  
<sup>157</sup> northern Davis County) are used to examine the occurrence of strong downslope winds be-  
<sup>158</sup> tween 1 October 1979 and 30 April 2012, the period for which European Centre for Medium-  
<sup>159</sup> Range Weather Forecasts (ECMWF) Re-Analysis (ERA)-Interim data are available (Dee  
<sup>160</sup> et al. 2011). KHIF has the longest and most reliable record of downslope windstorms of any  
<sup>161</sup> observing site along the Wasatch Front. Due to its position 5 km west of the Wasatch Front  
<sup>162</sup> base, and near the exit of Weber Canyon, KHIF frequently experiences easterly winds asso-  
<sup>163</sup> ciated with the Weber Canyon valley exit jet (Chrast et al. 2013), in addition to occasional  
<sup>164</sup> downslope windstorms. Holland (2002) found easterly wind gusts  $>23 \text{ m s}^{-1}$  about 1.5 times  
<sup>165</sup> per year during the entire observational period at the time (1953–1999), with more events  
<sup>166</sup> observed in the earlier years than the later ones. Over time, there has been suburban de-  
<sup>167</sup> velopment near KHIF, but not substantial enough to be responsible for the lower frequency  
<sup>168</sup> of events in these later years. The strongest wind gust recorded at KHIF was  $45 \text{ m s}^{-1}$  on  
<sup>169</sup> 4 April 1983. Holland (2002) derived composites of geopotential height on standard pres-  
<sup>170</sup> sure levels for 79 strong easterly wind events using coarse-resolution ( $2.5^\circ$  latitude/longitude

grid) National Centers for Environmental Prediction/National Center for Atmospheric Research reanalyses. Consistent with synoptic experience and forecasting practices at that time, the dominant composite signal described in that study was the development of a closed geopotential-height low on the 700-hPa surface, southwest of the Wasatch Mountains and centered near Las Vegas, NV. Receiving less attention in that study was the development to the north of the Wasatch Mountains of a composite geopotential-height ridge at 700 hPa, which extended from coastal Washington state, curving through Montana, to Wyoming. This cyclone–anticyclone structure is consistent with the life-cycle 1 (LC1) type of Rossby-wave breaking (Thorncroft et al. 1993), i.e., anticyclonic Rossby-wave breaking (ARWB).

A more conservative definition for strong Wasatch windstorms than that applied by Holland (2002) is used in this study. Observations at KHIF are taken automatically at hourly intervals, supplemented by occasional manual observations in between. A high wind event between October and April inclusive must satisfy the following criteria: (1) at least one KHIF observation with greater than  $15 \text{ m s}^{-1}$  sustained winds from an easterly direction between  $45^\circ$  and  $135^\circ$ ; and (2) ERA-Interim analyses must indicate a Rossby wave-breaking pattern (either anticyclonic as described above, or cyclonic LC2 type with a trough or closed low tilting in the east- and poleward direction, Thorncroft et al. 1993). One strong easterly-wind event at KHIF met criterion (1), but not (2), and was ignored. In addition, multiday events were reduced to a single day if they were associated with the same upper-level wave-breaking event. We applied these criteria across the entire observational record available (1953–2012), as in Holland (2002). Constrained by the availability of ERA-Interim analyses from 1 January 1979 to present, and avoiding inclusion of only half a season, these criteria led to identification of 13 distinct downslope windstorms between 1 October 1979 and 30 April 2012 inclusive. Table 2 shows their dates and sustained speeds and wind gusts.

The list of dates in Table 2 and the time series of their occurrence during 1979–2012 (Fig. 4) suggests that major downslope windstorms occurred once or twice every few years

until 1999. Subsequently, no major downslope windstorm occurred until the 1 December 2011 event investigated here. The intermittence of Wasatch windstorms, particularly the lack of windstorms in the first decade of this century, raises the question whether their occurrence is determined by fewer Rossby-wave breaking events over western North America, or more directly, by fewer crest-level easterly wind periods during winter. Strong and Magnusdottir (2008) developed an objective detection algorithm that generated a worldwide Rossby-wave-breaking climatology. Perhaps because their criteria allowed for weak and localized wave-breaking events, examination of their data as part of this study did not yield an obvious linkage of ARWB events to the occurrence of Wasatch windstorms. Figure 4 also shows the frequency of easterly (between  $45^\circ$  and  $135^\circ$ ) crest-level (700 hPa) winds over  $10 \text{ m s}^{-1}$  during each winter season (October–April inclusive) from the ERA Interim Reanalyses. Since crest-level strong-easterly-wind periods do occur in the years that downslope windstorms were absent, the seasonal frequency of easterly winds is not a good predictor for the rare occurrences of downslope windstorms within those seasons. Hence, we can offer no definitive explanation for the absence of major Wasatch downslope windstorms during the 2000–2010 period.

In our set of 13 major windstorms (Table 2), the hour of peak wind at KHIF varies from 0700 UTC to 1800 UTC. In general, the peak in widespread downslope winds along the Wasatch Front tend to occur near sunrise ( $\sim 1200$  UTC), since the dynamical forcing associated with the downslope winds is in phase at that time with the thermally forced Weber Canyon exit jet (Chrast et al. 2013). Hence, similar to Holland (2002), we show in Fig. 5 composites of 700-hPa geopotential height, assuming that the peak downslope wind occurs near 1200 UTC, and then composite conditions from 12 h earlier (0000 UTC) to 6 h after (1800 UTC). Southeastward progression of the tighter geopotential-height gradient associated with the breaking anticyclonic wave (e.g., Fig. 5b) marks the ARWB event, while the associated closed low deepens from 0000 to 1200 UTC followed by filling. The strongest easterly gradient winds across the Wasatch Front are at 1200 UTC.

When we compare the windstorm of 1 December 2011 to this climatological composite and to previous peak wind observations, we find it to be consistent with the upper-level signature of ARWB. It is also not only one of the strongest on record, but also the first in over ten years to match our criteria. In the next two subsections, we present observational and modeling data, respectively, to address why this was such a rare and damaging event.

*b. 1 December 2011 windstorm*

Figure 6 summarizes the synoptic evolution of the ARWB event on 1 December 2011 in ERA-Interim geopotential height and wind data on the 700-hPa surface. A small southwest-moving wave in the height field, accompanied by a jet maximum, moves faster than the mean flow towards the base of the trough between 0000 and 1200 UTC. The transport of cyclonic vorticity into the trough axis may contribute to the deepening of the closed low over the Nevada–Utah–Arizona borders: 700-hPa heights drop 60 m between 0000 and 0600 UTC, and fall another 30 m between 0600 and 1200 UTC. Lower-tropospheric cyclogenesis is often seen with LC1 baroclinic waves (Thorncroft et al. 1993). The closed-low center does not move far while its central height falls and the anticyclonic ridge breaks to the north. This clockwise pivoting of the breaking wave, and its slow southeastward progression, sustained a belt of  $25 \text{ m s}^{-1}$  easterly winds on the northwestern quadrant of the low-height center. By 1200 UTC, the crest of the Wasatch Front (at  $\sim 700 \text{ hPa}$ ) lies within this belt of strong easterly flow.

A longitude–pressure cross-section of zonal wind and potential temperature, taken on a west–east slice at 1200 UTC through ERA-Interim data, indicates a low-level easterly jet surmounted by a statically-stable layer to the east of the Wasatch Front (not shown). Farther aloft, cross-barrier flow reverses with height. As mentioned in section 1, both this elevated stable layer and the flow reversal are conducive to initiation and amplification of mountain waves.

The first northward mobile transect along the Wasatch Front between 0915 and 1015 UTC

251 captured the sudden onset of the strongest winds (Fig. 7). Departing from the UoU cam-  
252 pus, strong easterly winds were first encountered south of Centerville (UP028) with the  
253 peak winds found near Centerville. Strong easterly winds were also observed at the western  
254 mouth of the Weber River Canyon while speeds dropped off substantially farther east up  
255 the canyon. Union Pacific Railroad halted all train traffic at the eastern mouth of Weber  
256 Canyon, the end of the mobile-sensor transects in Fig. 7. Temperature and pressure mo-  
257 bile observations indicated near-uniform potential temperature at the base of the Wasatch  
258 Front; lower potential temperatures in the Weber River Canyon reflected the contribution of  
259 thermally-driven canyon flows to wind speed in this area (not shown). A 50-m tower located  
260 at the mouth of Weber River Canyon (Chrast et al. 2013) sampled winds at 3, 10, 30, and  
261 50 m above ground level. Mean wind speeds generally increase with sensor height during  
262 the period of strongest winds (1100–1900 UTC, not shown). However, due to the turbulent  
263 nature of the combined exit and downslope flows, peak winds are roughly equivalent in the  
264 10–50 m range; notably, 3-m wind gusts are occasionally as strong as those much farther  
265 aloft.

266 Figure 8a shows the time series of surface winds at KHIF on 1 December 2011 with most  
267 observations reported at hourly intervals. The strongest downslope winds were observed at  
268 this location during 1500–1800 UTC, preceded by a brief period of strong winds at 1200 UTC.  
269 Wind speed and direction at UFD04, a temporary station in Farmington, UT, located 1.5 km  
270 from the base of the Wasatch, captures the onset and cessation of the downslope windstorm  
271 at 0900 and 1900 UTC, respectively (Figure 8b). Peak intensity in winds at this location  
272 occurred ~1500–1600 UTC. These two stations (KHIF and UFD04) are representative of the  
273 windstorm’s characteristics along the foothills, including the time of peak winds occurring  
274 later farther north along the Wasatch Front. In contrast to the sudden onset and cessation  
275 of downslope winds in the valley, winds at the crest of the Wasatch as measured at Ogden  
276 Peak (OGP, Fig. 8c) show a persistent easterly flow with winds increasing in intensity until  
277 late afternoon.

278 Vertical profiles of wind, temperature, and moisture, collected by rawinsondes launched  
279 twice-daily at KSLC during prior windstorms, have exhibited primarily the prevailing synop-  
280 tic flow combined with complex downstream effects of the flow over the Wasatch Range. Fig-  
281 ure 9 shows the KSLC sounding launched at  $\sim$ 1100 UTC with a nominal observation time of  
282 1200 UTC. The profile exhibits features typically observed at KSLC during a Wasatch wind-  
283 storm: (1) no indication of downslope winds near the surface (i.e., weak low-level southerly  
284 drainage flow down the Salt Lake Valley towards the Great Salt Lake); (2) strong easterly  
285 winds below and extending above crest level (700 hPa); (3) easterly winds weakening aloft  
286 with limited cross-barrier flow at 500 hPa; (4) little moisture evident in the profile; (5) a  
287 small surface-based inversion with a well-mixed layer extending upwards to  $\sim$ 750 hPa; (6)  
288 evidence of strong turbulence between 750 and 700 hPa with superadiabatic lapse rates; and  
289 (7) a capping inversion layer near crest ( $\sim$ 690 hPa) with an adiabatic layer above that level  
290 to 650 hPa.

291 The UoU team planned to launch rawinsondes upstream and downstream of the Wasatch  
292 at roughly the same time as the nearby NWS launch at KSLC ( $\sim$ 1100 UTC), and then to  
293 continue operations as conditions warranted. These additional launches were intended to  
294 describe the flows upstream and immediately downstream of the terrain where the strongest  
295 winds were expected. Upstream launches near Morgan, UT were made at the nominal  
296 observation times of 1200, 1500, and 1800 UTC (i.e., balloons released at 1100, 1400, and  
297 1700 UTC, respectively). Since short-period communication failures between the radio base  
298 station and the 1200 and 1500 UTC sondes near Morgan created small data gaps of 25–75 hPa  
299 in depth, the 1800 UTC profile is shown in Fig. 10a. The automated algorithms provided  
300 by the rawinsonde manufacturer tend to smooth excessively the wind observations, hence  
301 the following figures use raw, unsmoothed wind data. Upstream of the Wasatch Range, the  
302 lowest 750 m is well-mixed and nearly adiabatic, below a string of stable layers up to 5 km.  
303 A particularly strong inversion is evident at  $\sim$ 3250 m, an elevation roughly 500 m above the  
304 crest of the Wasatch in this area, which caps a layer with higher relative humidity and the

305 strongest easterly winds ( $\sim 30 \text{ m s}^{-1}$ ) observed at this time. Above the highest inversion,  
306 winds are substantively weaker, and relative humidity is lower. Notably, easterly winds are  
307 observed throughout the profile below 5000 m.

308 A day previously, the UoU team selected a park in Centerville, UT for a lee-side raw-  
309 insonde launch. Fortunately, its position was within the core of strongest wind observed  
310 during the event, located immediately upwind ( $\sim 200 \text{ m}$ ) of the UDOT tower (CEN) and  
311 Union Pacific Railroad tower (UP028), themselves immediately west of the Interstate 15  
312 freeway (see Fig. 2). Sound-barrier walls east of the freeway bracket the park on its north  
313 and south edges and contributed to channeling of the flow. Several trucks tipped over as  
314 they passed northward from the protection of the sound barrier into the unprotected zone  
315 on the freeway, as well as on the adjacent frontage road. It was under these extremely harsh  
316 conditions that the UoU team successfully launched a rawinsonde at 1100 UTC at the park.  
317 The balloon initially travelled nearly horizontally towards the freeway, before gaining alti-  
318 tude and clearing trees located at the edge of the frontage road. Vertical profiles of potential  
319 temperature, relative humidity, and wind speed and direction from the 1200 UTC Centerville  
320 sounding are shown in Fig. 10b. Two small communication gaps occurred during the as-  
321 cent, one at 3050–3200 m, and another at 3400–3500 m. The immediate surface layer (lowest  
322 50–60 m) is characterized by lower potential temperature and horizontal winds approaching  
323  $40 \text{ m s}^{-1}$ , consistent with the nearby surface wind gust observations of  $\sim 36 \text{ m s}^{-1}$  at UP028  
324 at this time. Following Armi and Mayr (2011), this layer is referred to as the “downslope  
325 underflow”.

326 A sharp inversion ( $5.7^\circ\text{C}$  increase in  $\sim 3.5 \text{ hPa}$ ) at 3300 m caps a turbulent layer con-  
327 taining adiabatic, superadiabatic, and weakly stable sublayers between 1700 m and 3300 m.  
328 Relative humidity increases to 90% through this depth and falls sharply through the in-  
329 version. Winds again increase to over  $30 \text{ m s}^{-1}$  in the inversion layer, and rotate above the  
330 inversion to sharply-reduced cross-barrier flow above 3750 m. This rotation is not evident  
331 upstream near Morgan, and may therefore be self-induced. The sharp inversion is consis-

332 tent with flow separation as the air crosses the Wasatch; the downslope underflow descends  
333 steeply along the slope, while another strong easterly current flows outward near crest level  
334 ( $\sim 3300$  m). All three sondes upstream of the Wasatch Range detected the strongest winds  
335 ( $25\text{--}30 \text{ m s}^{-1}$ ) at 3100–3200 m, consistent with the strong crest-level winds observed near the  
336 inversion layer above Centerville.

337 Figure 11 contrasts the ascent rates at  $\sim 1\text{--}2$ -s intervals experienced by the Morgan and  
338 Centerville rawinsondes. The ascent rate near Morgan, averaged from surface to 3300 m, is  
339  $4.8 \text{ m s}^{-1}$ , which is roughly what would be expected given the amount of helium used in the  
340 balloon (e.g., the 1200 and 1500 UTC sondes had average ascent rates of 4.5 and  $5.3 \text{ m s}^{-1}$ ,  
341 respectively). The Centerville rawinsonde, using a similar volume of helium, experienced  
342 vastly different conditions from that near Morgan. Consistent with visual tracking of the  
343 Centerville sonde until lost in the dark, the buoyancy imparted by the helium was initially  
344 negated by descending motions, resulting in a near-horizontal trajectory. Then, the rawin-  
345 sonde ascended at increasingly rapid rates approaching  $25 \text{ m s}^{-1}$  through the superadiabatic  
346 layer. Vertical speeds then decreased up to 2900 m. The balloon made no headway verti-  
347 cally through the sharp inversion, and at times descended in that layer, which led to a large  
348 number of observations in this vicinity. Once clear of this layer, the balloon ascended at an  
349 average rate of  $4.6 \text{ m s}^{-1}$ . Subtracting this mean ascent rate from the observed rate yields a  
350 crude estimate of peak vertical velocities  $O(20 \text{ m s}^{-1})$  upwards and  $O(7.5 \text{ m s}^{-1})$  downwards.

351 The violent ascent and descent of the balloon is consistent with visual evidence after  
352 sunrise of rotors (low-level vortices with horizontal axes parallel to the ridgeline in the lee of  
353 mountain range; Doyle and Durran 2002). Satellite images and photos indicate an upstream  
354 cloud deck over the Wasatch evaporating in the air descending down the lee slope with  
355 distinctive rotor clouds evident to the west of the base of the slope (not shown). The quasi-  
356 uniform horizontal distance from the crest to the location of the rotor clouds is  $\sim 10$  km (3–  
357 5 km from the base of the mountains). The superadiabatic lapse rate in the layer 2000–2500 m  
358 may result from the formation of rotor clouds and then subsequent evaporative cooling of

359 the air when the clouds dissipate. Aircraft, dropsonde, and lidar observations from the  
360 Terrain-Induced Rotor Experiment (T-REX) provide more comprehensive depictions of the  
361 turbulence and rotors present in the lee of the Sierra Mountains during downslope windstorms  
362 (Armi and Mayr 2011; Kühnlein et al. 2013). For example, aircraft and lidar observations  
363 during T-REX detected vertical velocities greater than  $10\text{--}15\text{ m s}^{-1}$  in the ascending air  
364 beneath rotor clouds.

365 *c. Control simulation*

366 The ability of a numerical simulation to capture the core features observed during this  
367 windstorm is now examined. A numerical simulation, referred to as the Control simulation,  
368 was performed with the WRF model initialized from the NAM-model analysis at 0600 UTC  
369 29 November 2011, and forced thereafter on the outermost boundary by NAM analyses  
370 updated every 6 h. The Control simulation is initialized far enough in advance for mesoscale  
371 circulations to develop freely, and continues for 72 h to encompass the entire downslope  
372 windstorm event. The simulated 700-hPa geopotential height fields for 0000–1800 UTC 1  
373 December (42–60 h into the simulation) are shown in Fig. 12, taken from the largest (12-km)  
374 WRF domain. The model captures the synoptic-scale structure of this ARWB event, with  
375 a ridge developing and extending southeastward from northern Idaho into Wyoming, while  
376 the cut-off low becomes centered near the southern tip of Nevada. Relative to the 700-hPa  
377 circulation depicted in the ERA-Interim reanalyses, values of geopotential height simulated  
378 by the model are elevated by  $\sim 60\text{ m}$  everywhere, but the modeled height gradients are similar  
379 to those analyzed, particularly in the vicinity of the Wasatch Front. However, the model  
380 simulation is slower in its development of the ARWB event, with the cut-off low-height center  
381 deepening until 1800 UTC.

382 Observed surface wind speeds near the Wasatch Front at 1200 UTC and 2100 UTC are  
383 superimposed on the surface wind fields simulated by the model in Fig. 13. The simulated  
384 winds are comparable to those observed near the base of the lee slopes of the Wasatch

Mountains at 1200 UTC, including the localized maximum near Centerville. By later in the day (2100 UTC), the model has shifted the strongest winds farther north, but the simulated winds appear too strong compared to observations. The winds along the crest in the model are lower than those observed; for example, simulated wind speeds were  $10\text{--}15 \text{ m s}^{-1}$ , while the winds observed at OGP and other crest-level stations at Snowbasin Ski Resort (not shown) were greater than  $20 \text{ m s}^{-1}$  (see also Fig. 8c). As will be shown in greater detail later, the model tends to accelerate the flow down the slopes of the Wasatch Mountains more strongly than is likely taking place. The WRF model develops rotors and trapped waves, and these phenomena appear in the valley surface winds at 2100 UTC as bands of increased and decreased winds in bands oriented parallel to the upstream terrain. In this 1.3-km domain simulation, strong winds do not extend out over the Great Salt Lake, whereas operational NWS 4-km WRF model forecasts (not shown) suggested a westward extension of  $25\text{--}30 \text{ m s}^{-1}$  gusts as far west as Antelope Island (labelled AI in Fig. 13).

The time evolution of wind speed and direction during the simulated downslope wind-storm is now related in Fig. 14 to that observed at Farmington (UFD04) (previously shown in Fig. 8b). The Control simulation shows remarkable agreement with the observations regarding the timing and general evolution of the intensity of the surface winds. However, the simulated windstorm continues for  $\sim 2$  h longer than that observed.

Figure 9 compares the vertical profiles of temperature, moisture, and wind at KSLC at 1200 UTC from the Control simulation to the observed sounding. The model captures the basic vertical structure, but the simulated vertical profiles differ from those observed in several key respects: (1) surface westerly return flow rather than decoupled down-valley winds; (2) peak easterly flow near the base of a stable layer at 775 hPa relative to that observed near 700 hPa; (3) deep well-mixed layer between 750–550 hPa with near-zero cross-barrier flow at 600 hPa, and more stable conditions and weak cross-barrier flow above  $\sim 475$  hPa; and (4) generally lower dewpoint temperature throughout the troposphere.

To further evaluate the control simulation, we now present cross-sections of potential

temperature and horizontal wind from the control simulation. The first cross-section lies along the southwest–northeast (A–B) transect shown in Fig. 1, starting from the Great Salt Lake, through Centerville and terminating near Lyman, WY (Fig. 15). The wind components from the WRF model are rotated  $20^\circ$  counterclockwise to create plane-parallel winds at all levels. Note that the terrain height is lower in the model than that observed: as a result of smoothing, the model’s Wasatch Range is  $\sim 250$  m lower than the actual terrain.

In the top panel of Fig. 15, at 1200 UTC,  $20 \text{ m s}^{-1}$  flow from the northeast (right to left in the figure) approaches the Wasatch Front, and then plunges sharply into the valley as a downslope windstorm. Note how the colder air (lower potential temperature) pools in the upstream valley, effectively creating an unobstructed horizontal pathway for the low-level easterly jet. Downstream of the Wasatch crest, strong winds continue for more than 10 km along the valley floor before forming a rotor. Under this first rotor,  $5\text{--}10 \text{ m s}^{-1}$  westerly winds oppose the windstorm easterlies. The area of strong surface winds is broader than observed, i.e., observations suggest the rotor clouds and return flow begin roughly 10 km from the crest, while the model shifts that farther west. In the bottom panel, at 2100 UTC, the upstream stable layer has intensified as a result of both terrestrial heating and continued cold advection in the planetary boundary layer at  $\sim 3000$  m. This enhances the formation of mountain waves above the upstream terrain. The formation of rotors at this time occurs closer to the crest, though it is important to note that these images are merely snapshots; the locations of the non-linear internal gravity waves shift with time as a result of dynamical and turbulent processes (e.g., Hertenstein 2009).

As evident in the Skew-T diagram for KSLC (Fig. 9), the model’s strongest easterly winds tend to be at a lower height over the terrain than observed. This may explain the model’s tendency to confine flow to follow the terrain slope more closely than observed, i.e., the elevated flow extending westward away from the crest is missing from the model. Note also that the simulated winds immediately above the Wasatch crest are weak (see also Fig. 13), which contributes to flow descending at a steeper angle associated with the lee waves. The

439 model also does not capture the strong capping inversion above the rotor observed near  
440 Centerville.

441 Cross-sections of vertical motion indicate ascent within the rotor at 1200 UTC is on the  
442 order of  $20\text{--}30 \text{ m s}^{-1}$  (not shown), which is broadly consistent with the ascent rate estimated  
443 from the Centerville rawinsonde at this time. However, the overall structure of the simulated  
444 downslope windstorm is too intense, relative to that inferred from the Centerville sounding  
445 and other observational evidence. The strong subsidence, 2-km plunging of the isentropes,  
446 and extreme drying in the lee of the mountains is not likely to have taken place during  
447 this event. The lee waves continue to amplify through the time of the later cross-section as  
448 evident by the isentropes in Fig. 15 at 2100 UTC.

449 Cross-sections perpendicular to the upstream flow (i.e., roughly north–south across a  
450 swath of lower terrain in Wyoming and extending into the Uinta mountains; C–D in Fig. 1)  
451 are generated by rotating the wind components  $\sim 5^\circ$  counterclockwise (Fig. 16). At 1200 UTC,  
452 the simulation generates a barrier-jet-like core of  $15\text{--}20 \text{ m s}^{-1}$  easterly winds to the north of  
453 the Uinta mountains. By 2100 UTC, the strong easterly flow has extended farther north, as  
454 the cut-off low reaches a position directly south of the Wasatch Front. These factors may  
455 help to explain the observed northward progression of strong winds along the Wasatch Front  
456 as a result of the more windstorm-favorable easterlies extending farther north later in the  
457 day.

458 *d. Sensitivity to Uinta Mountains*

459 The Uinta Mountains are a substantial barrier and have the distinction of being the  
460 highest mountain range (a crest line above 3000 m) in the contiguous United States oriented  
461 in the east–west direction. Their location south of the open expanses of western Wyoming  
462 may contribute to channeling easterly winds towards the Wasatch Mountains. To test the  
463 sensitivity of the windstorm’s strength and occurrence to the upstream terrain, we now  
464 present results of a modeling experiment (referred to as the No-Uinta simulation) in which

465 the Uinta Mountains are flattened. Following similar WRF-terrain modifications by West  
466 and Steenburgh (2011) and Alcott and Steenburgh (2013), the impact of the Uinta Mountains  
467 on the 1 December 2011 Wasatch downslope windstorm is investigated by completing a  
468 simulation in which the terrain height of the Uintas above 2300 m is lowered to that elevation  
469 on the 4- and 1.3-km domains (the Uintas remain unchanged on the 12-km domain to  
470 minimize discontinuities on the largest scales). This has two additional impacts: (1) the  
471 resultant void is replaced by a volume of standard-atmosphere air, and (2) soil temperatures  
472 are replaced with the deep-soil values in places where the upper soil layers have been removed.  
473 Due to the strong dynamical forcing of this event, these two changes are unlikely to greatly  
474 affect the simulation in comparison to the changes arising from the altered terrain. The use  
475 of two-way feedback between the nested domains implies that the Uintas' presence in the  
476 outer domain may still be felt to some extent on the inner domains, i.e., the impact of their  
477 removal may be underestimated here.

478 Figure 17 shows the zonal wind difference (No-Uinta minus Control) after reducing the  
479 height of the Uinta mountains. At 1200 UTC, there is a strong increase–decrease dipole  
480 centered near Salt Lake City (marked by SLC). North of Salt Lake City, easterly winds  
481 have been markedly reduced by the removal of the Uinta Mountains (elevations of which are  
482 contoured in red). The decreased easterly flow north of the Uinta mountains' former position  
483 supports the hypothesis that the Uintas obstruct southward flow and create a barrier jet  
484 towards the northern Wasatch Front. Conversely, easterly winds have strengthened to the  
485 south of Salt Lake City, particularly around the city of Provo in the southern Wasatch Front.  
486 Without the Uintas, the northeasterly flow from Wyoming is unimpeded and plunges over  
487 the Wasatch farther south as a downslope windstorm in that region.

488 Later at 2100 UTC—with or without the Uinta mountains—there are strong easterly  
489 winds in the northern Wasatch Front, confirming the importance of the orientation of large-  
490 scale midtropospheric winds; i.e., when the large-scale flow becomes more easterly, the impact  
491 of the blocking by the Uintas is lessened. The reduced elevation of the Uintas allows the

492 windstorm to continue in the southern Wasatch Front at this time. Overall, an increased east-  
493 erly component appears to initiate mountain waves more easily along the northern Wasatch  
494 Front. In contrast, the presence of the Uintas likely shields the southern Wasatch Front from  
495 damaging winds on many occasions. The time series of simulated surface wind at UFD04,  
496 with (green) and without (red) the Uintas, are shown in Fig. 14, and corroborates the sen-  
497 sitivity of valley wind speed to the orientation of the large-scale flow. Without the Uintas,  
498 the downslope easterly flow is weaker until the model’s synoptic-scale flow becomes more  
499 easterly after 1500 UTC.

500 Cross-sections are now shown as before, but with the Uinta mountains reduced in eleva-  
501 tion (Figs. 18 and 19). While the stability is comparable, a weaker jet crosses the Wasatch  
502 crest at 1200 UTC (Fig. 18). This results in weaker mountain waves, which do not penetrate  
503 to the floor of the Wasatch Front. At 2100 UTC, wind speeds are still slightly weaker than  
504 the Control run, though strong winds now reach the valley floor. A comparison of verti-  
505 cal wind speeds from the No-Uinta and Control simulations indicates the weaker mountain  
506 wave pattern downstream of the Wasatch crest at both times in the No-Uinta simulation  
507 (not shown). The north–south No-Uinta cross-section (Fig. 19) maintains a core of strong  
508 easterlies at 1200 UTC from the control run, though this core is more elongated than the  
509 Control.

## 510 4. Summary

511 This study documented the severe downslope windstorm in northern Utah on 1 December  
512 2011, which caused over \$75m damage along the Wasatch Front. This event had the second-  
513 highest maximum wind speed and gust recorded at KHIF since 1979. A brief climatological  
514 analysis of earlier events highlighted the lack of downslope windstorms in this area in the  
515 period 2000–2010. Identifying the causes for this temporal gap has been inconclusive. There  
516 was no strong evidence to suggest that crest-level easterly winds were simply less frequent

517 during the 2000–2010 period (Fig. 4) nor that ARWB events were less frequent.

518 The 1 December 2011 downslope windstorm occurred as a result of a well-defined synoptic  
519 setting, which can be summarized as follows:

- 520 • An ARWB event over western North America established the prevailing easterly flow in  
521 the midtroposphere over the Wasatch Mountains. The stalling of the associated mid-  
522 tropospheric cut-off low over southern Nevada maintained this easterly flow's position  
523 over the Wasatch range, and sustained the downslope windstorm until early afternoon  
524 local time.
- 525 • The gradient easterly wind near crest-level (700 hPa) developed rapidly between 0600  
526 and 1200 UTC, initially oriented from the northeast, but veering by 1800 UTC to be  
527 more directly from the east before weakening after 2100 UTC.
- 528 • Common to downslope windstorms in other areas, mountain waves generated from the  
529 easterly flow orthogonal to the Wasatch may have been reflected back towards the  
530 surface by the stable layer (Smith 1985). This process may have also generated its own  
531 critical layer, seen in observational and numerical-simulation data, where the cross-  
532 barrier component to the flow falls to zero (Peltier and Clark 1979) in downstream,  
533 and not upstream, profiles.
- 534 • As the large-scale lower-tropospheric height gradient from Wyoming to Nevada in-  
535 creased during the day, cold air surged across Wyoming. The Uinta Mountains may  
536 have shunted initial northeasterly flow towards the Wasatch Front, leading to a barrier-  
537 jet-like feature associated with strong cold advection. Cold air filled in the lowest de-  
538 pressions allowing the barrier jet to continue downstream (and immediately upstream  
539 of the Wasatch Mountains at Morgan, UT) at an elevation of a few hundred meters  
540 above crest level.

541 The localized nature of Wasatch downslope windstorms was readily apparent during this  
542 event. The downslope winds began abruptly at ∼0900 UTC resulting from the initial push of

543 the easterly flow across the Wasatch Mountains and trapped beneath the stable layer farther  
544 aloft. The strongest winds were observed at  $\sim$ 1500 UTC in Centerville, and ended abruptly  
545 in that area after 1900 UTC. A feature of this event uncommon to previous ones was the  
546 progression through midday (local time) of the strongest winds, and the subsequent damage  
547 farther north. The cross-barrier flow measured at OGP immediately above the locations  
548 in Weber County where damage occurred (including the Weber State University campus)  
549 continued to increase until late afternoon as a result of the synoptic-scale shifts in the large-  
550 scale flow. Observations during the morning from a vehicle-mounted sensor filled the spatial  
551 gaps between the automated observing sites along the Wasatch Front. Although peak winds  
552 were observed at numerous favored locations (fewer upstream obstructions, etc.), there was  
553 a general uniformity of the flow spilling over the mountains and reaching their base (i.e.,  
554 widespread strong easterly winds of quasi-constant potential temperature that was close  
555 to values observed at jet level upstream of the Wasatch, and low dewpoint temperature).  
556 Lower temperatures within Weber River Canyon, sampled by the vehicle-mounted sensor  
557 and nearby stations, indicated the additional effects of low-level gap flows travelling through  
558 this canyon.

559 The data from the rawinsonde released at 1100 UTC in Centerville revealed a clear un-  
560 derflow near the surface (Armi and Mayr 2011) before the sonde ascended rapidly within a  
561 rotor. A sharp subsidence inversion capped the rotor with strong winds observed at that  
562 level. This bifurcation of the strongest winds (at the surface and at the level of the inversion)  
563 is similar to that found in large-eddy simulations of downslope flows (e.g., Hertenstein 2009).  
564 The characteristics of a self-induced critical layer farther aloft may also be evident (Peltier  
565 and Clark 1979). The localized nature of the characteristic features of downslope windstorms  
566 below the crest of the Wasatch Range found near Centerville is apparent by comparing the  
567 vertical profiles at Centerville to the sounding at KSLC. The KSLC sounding has typical  
568 morning downvalley flows, decoupled from a well-mixed layer below crest-level, and hints of  
569 strong turbulence below a strong inversion near 700 hPa. Not surprisingly, the two profiles

570 of temperature, moisture, and wind are quite similar to one another above crest level.

571 Even with the relatively-rich observational dataset available to examine this windstorm,  
572 a high-resolution WRF numerical simulation forced by NAM-analyzed conditions on the  
573 outer boundary provides critical information on the dynamical and thermodynamical struc-  
574 ture associated with the event. The WRF simulation captured many of the synoptic-scale  
575 features evident from the ERA-Interim Reanalyses. However, the breaking of the Rossby  
576 wave in the Control simulation was slightly slower; deepening of the cut-off low in the model  
577 simulation continued until 1800 UTC over southern Nevada, whereas at this point, ERA-  
578 Interim reanalysis showed filling of the low to have already started. The model 10-m winds  
579 along the Wasatch Front had many similarities to those observed, including the location of  
580 the maximum winds. However, the model's 10-m winds at crest level tended to be weaker  
581 than those observed along the crest. The model's response to the flow across the Wasatch  
582 barrier beneath the strong stable layer is to develop mountain waves larger in amplitude  
583 than was likely present. This results in model vertical profiles at the western base of the  
584 Wasatch Mountains that are more akin to extreme-amplitude mountain-wave windstorms  
585 (e.g., Grubišić and Billings 2008). The model creates a band of dry air, flowing parallel  
586 down the terrain along isentropes, from high above the model terrain and plunging close to  
587 the surface. A lateral jet, evident in the Centerville observed profile near crest level, does  
588 not form in the model simulations.

589 Following similar WRF-terrain modifications by West and Steenburgh (2011) and Alcott  
590 and Steenburgh (2013), we investigated whether the Uinta Mountains (a major barrier to  
591 meridional flow across the Wyoming–Utah border) steer northeasterly lower-tropospheric  
592 flow more directly towards the Wasatch Mountains, potentially supporting windstorms in  
593 Davis County earlier in the synoptic pattern progression. If the Uinta Mountains in the WRF  
594 model are reduced in elevation comparable to that found over much of western Wyoming,  
595 then southwestward cold advection spills farther south across the Wasatch Front in the  
596 absence of the blocking terrain. However, as the synoptic-scale flow later in the day veers

597 towards a more easterly direction, then the blocking effect of the Uinta Mountains is lessened.

598 The NWS first mentioned a possible downslope windstorm along the Wasatch Front  $\sim$ 90 h  
599 before its onset. Confidence in this forecast was supported by operational deterministic  
600 high-resolution model runs. In contrast, Reinecke and Durran (2009) evaluated ensemble  
601 forecasts of downslope windstorms in the lee of the Sierra Mountains of California and  
602 estimated predictability timescales of  $O(12\text{ h})$  for their two case studies. As summarized by  
603 Doyle et al. (2013), numerous studies have suggested that error growth might be reduced,  
604 and predictability enhanced, for mesoscale phenomena such as downslope windstorms as  
605 a result of terrain-flow interactions. Furthermore, events that are strongly coupled with  
606 larger-scale (i.e., typically more-predictable) phenomena such as ARWB events may inherit  
607 some predictability tendency from the larger scales, which may help (Palmer 1993) or hinder  
608 (Durran and Gingrich 2014) smaller-scale forecasts. We will attempt in a separate study  
609 to understand the apparent enhanced predictability for this downslope windstorm event  
610 with 11-member ensembles from the Global Ensemble Forecast System Reforecast, Version  
611 2 (Hamill et al. 2013), using ensemble reforecasts starting as early as 25 November 2011  
612 (150 h before the onset of the strong winds).

613 *Acknowledgments.*

614 We thank Professors Courteney Strong and Jim Steenburgh for useful suggestions; Erik  
615 Crosman and Trevor Alcott for much valuable advice; Roger Akers, Chris Ander, Erik Cros-  
616 man, Alex Jacques, Matt Lammers, Nola Lucke, Wil Mace, and Trevor Alcott, all for assis-  
617 tance in collecting data during the windstorm; the Center for High-Performance Computing  
618 at the University of Utah for provision of, maintenance of, and assistance with the super-  
619 computers. This research was supported by NOAA/NWS Collaborative Science, Technology,  
620 and Applied Research Program Grant NA10NWS4680005.

## REFERENCES

- 623 Alcott, T. and W. J. Steenburgh, 2013: Orographic influences on a Great Salt Lake-effect  
 624 snowstorm. *Mon. Wea. Rev.*, **141**, 2432–2450.
- 625 Armi, L. and G. J. Mayr, 2011: The descending stratified flow and internal hydraulic jump  
 626 in the lee of the Sierras. *J. Appl. Meteor. Climatol.*, **50**, 1995–2011.
- 627 Chrust, M. F., C. D. Whiteman, and S. W. Hoch, 2013: Observations of thermally driven  
 628 wind jets at the exit of Weber Canyon, Utah. *J. Appl. Meteor. Climatol.*, **52**, 1187–1200.
- 629 Dee, D. P., S. M. Uppala, A. J. Simmons, P. Berrisford, P. Poli, S. Kobayashi, U. Andrae,  
 630 M. A. Balmaseda, G. Balsamo, P. Bauer, P. Bechtold, A. C. M. Beljaars, L. van de Berg,  
 631 J. Bidlot, N. Bormann, C. Delsol, R. Dragani, M. Fuentes, A. J. Geer, L. Haimberger,  
 632 S. B. Healy, H. Hersbach, E. V. Hólm, L. Isaksen, P. Kållberg, M. Köhler, M. Matricardi,  
 633 A. P. McNally, B. M. Monge-Sanz, J.-J. Morcrette, B.-K. Park, C. Peubey, P. de Rosnay,  
 634 C. Tavolato, J.-N. Thépaut, and F. Vitart, 2011: The ERA-Interim reanalysis: configu-  
 635 ration and performance of the data assimilation system. *Q. J. Roy. Meteor. Soc.*, **137**,  
 636 553–597.
- 637 Doyle, J. and D. Durran, 2002: The dynamics of mountain-wave-induced rotors. *J. Atmos.  
 638 Sci.*, **59**, 186–201.
- 639 Doyle, J., C. Epifanio, A. Persson, P. Reinecke, and G. Zängl, 2013: Mesoscale modeling over  
 640 complex terrain: numerical and predictability perspectives. *Mountain Weather Research  
 641 and Forecasting: Recent Progress and Current Challenges*, F. Chow, S. De Wekker, and  
 642 B. Snyder, eds., Springer, 531–590.
- 643 Durran, D. R. and M. Gingrich, 2014: Atmospheric predictability: Why butterflies are not  
 644 of practical importance. *J. Atmos. Sci.*, **71**, 2476–2488.

- 645 Grubišić, V. and B. J. Billings, 2008: Climatology of the Sierra Nevada mountain-wave  
646 events. *Mon. Wea. Rev.*, **136**, 757–768.
- 647 Hamill, T. M., G. T. Bates, J. S. Whitaker, D. R. Murray, M. Fiorino, T. J. Galarneau,  
648 Y. Zhu, and W. Lapenta, 2013: NOAA’s second-generation global medium-range ensemble  
649 reforecast data set. *Bull. Am. Meteorol. Soc.*, **94**, 1553–1565.
- 650 Hertenstein, R. F., 2009: The influence of inversions on rotors. *Mon. Wea. Rev.*, **137**, 433–  
651 446.
- 652 Holland, L., 2002: *Downslope windstorms along the Wasatch Front*. M.S. Thesis, University  
653 of Utah, 86 pp.
- 654 Horel, J., T. Potter, L. Dunn, W. Steenburgh, M. Eubank, M. Splitt, and D. Onton, 2002a:  
655 Weather support for the 2002 Winter Olympic and Paralympic Games. *Bull. Amer. Me-  
656 teor. Soc.*, **83**, 227–240.
- 657 Horel, J., M. Splitt, L. Dunn, J. Pechmann, B. White, C. Ciliberti, S. Lazarus, J. Slemmer,  
658 D. Zaff, and J. Burks, 2002b: Mesowest: cooperative mesonet in the western United  
659 States. *Bull. Amer. Meteor. Soc.*, **83**, 211–225.
- 660 Jiang, Q. and J. D. Doyle, 2008: Diurnal Variation of Downslope Winds in Owens Valley  
661 during the Sierra Rotor Experiment. *Mon. Wea. Rev.*, **136**, 3760–3780.
- 662 Jones, C., J. Colton, R. McAnelly, and M. Meyers, 2002: An examination of a severe downs-  
663 lope windstorm west of the Colorado Park Range. *Natl. Weather Dig.*, **26**, 73–81.
- 664 Kühnlein, C., A. Dörnbrack, and M. Weissmann, 2013: High-Resolution doppler lidar ob-  
665 servations of transient downslope flows and rotors. *Mon. Wea. Rev.*, **141**, 3257–3272.
- 666 Lareau, N. P., E. Crosman, C. D. Whiteman, J. Horel, S. W. Hoch, W. O. J. Brown, and  
667 T. W. Horst, 2013: The Persistent Cold-Air Pool Study. *Bull. Amer. Meteor. Soc.*, **94**,  
668 51–63.

- 669 Lawson, J., 2013: *Analysis and predictability of the 1 December Wasatch downslope wind-*  
670 *storm*. M.S. Thesis, University of Utah, 84 pp.
- 671 Lilly, D. K. and E. J. Zipser, 1972: The front range windstorm of 11 january 1972: a  
672 meteorological narrative. *Weatherwise*, **25**, 56–63.
- 673 Markowski, P. and Y. Richardson, 2010: *Mesoscale Meteorology in Mid-latitudes*. Wiley-  
674 Blackwell, 407 pp.
- 675 Mass, C. and M. Albright, 1985: A severe windstorm in the lee of the cascade mountains of  
676 washington state. *Mon. Weather Rev.*, **113**, 1261–1281.
- 677 Miller, P. and D. Durran, 1991: On the sensitivity of downslope windstorms to the asym-  
678 metry of the mountain profile. *J. Atmos. Sci.*, **48**, 1457–1473.
- 679 O'Donoghue, A. J., 2012: Remembering the winds of 2011: Utah's 'most devastating wind  
680 event' in decades happened 1 year ago. *Deseret News*, Salt Lake City.
- 681 Palmer, T., 1993: Extended-range atmospheric prediction and the Lorenz model. *Bull. Amer.*  
682 *Meteor. Soc.*, **74**, 49–65.
- 683 Peltier, W. and T. Clark, 1979: The evolution and stability of finite-amplitude mountain  
684 Waves. Part II: surface wave drag and severe downslope windstorms. *J. Atmos. Sci.*, **36**,  
685 1498–1529.
- 686 Reinecke, P. and D. Durran, 2009: Initial-condition sensitivities and the predictability of  
687 downslope winds. *J. Atmos. Sci.*, **66**, 3401–3418.
- 688 Richner, H. and P. Hächler, 2013: Understanding and forecasting Alpine Foehn. *Mountain*  
689 *Weather Research and Forecasting: Recent Progress and Current Challenges*, F. Chow,  
690 S. De Wekker, and B. Snyder, eds., Springer, 219–260.
- 691 Smith, R., 1985: On severe downslope winds. *J. Atmos. Sci.*, **42**, 2597–2603.

- 692 Strong, C. and G. Magnusdottir, 2008: Tropospheric Rossby wave breaking and the  
693 NAO/NAM. *J. Atmos. Sci.*, **65**, 2861–2876.
- 694 Thorncroft, C. D., B. Hoskins, and M. McIntyre, 1993: Two paradigms of baroclinic-wave  
695 life-cycle behaviour. *Q. J. Roy. Meteor. Soc.*, **119**, 17–55.
- 696 Vosper, S., 2004: Inversion effects on mountain lee waves. *Q. J. Roy. Meteor. Soc.*, **130**,  
697 1723–1748.
- 698 Wang, T.-A. and Y.-L. Lin, 1999: Wave ducting in a stratified shear flow over a Two-  
699 Dimensional mountain. part II: Implications for the development of High-Drag states for  
700 severe downslope windstorms. *J. Atmos. Sci.*, **56**, 437–452.
- 701 Welch, W. and D. Rice, 2011: 100-mph Santa Ana winds whip Southwest. *USA Today*.
- 702 West, G. L. and W. Steenburgh, 2011: Influences of the Sierra Nevada on Intermountain  
703 cold-front evolution. *Mon. Wea. Rev.*, **139**, 3184–3207.
- 704 Whiteman, C. D., 2000: *Mountain Meteorology: Fundamentals and Applications*. Oxford  
705 University Press, USA, New York, 355 pp.
- 706 Zhong, S., J. Li, C. David Whiteman, X. Bian, and W. Yao, 2008: Climatology of high wind  
707 events in the owens valley, california. *Mon. Weather Rev.*, **136**, 3536–3552.

<sub>708</sub> **List of Tables**

<sub>709</sub> 1	Parameterization schemes used in numerical modeling configuration.	30
<sub>710</sub> 2	Downslope windstorm events at KHIF as defined by this study.	31

Table 1: Parameterization schemes used in numerical modeling configuration.

<b>Parameterization</b>	<b>Scheme</b>
<b>Microphysics</b>	WRF Single-Moment 3-class Scheme
<b>Longwave Radiation</b>	RRTM Scheme
<b>Shortwave Radiation</b>	Dudhia Scheme
<b>Surface Layer</b>	MM5 Similarity
<b>Land Surface</b>	Noah Land Surface Model (with snow effect)
<b>Urban Surface</b>	Switched off
<b>Planetary Boundary Layer</b>	Yonsei University Scheme
<b>Cumulus Parameterization</b>	Kain-Fritsch Scheme (12-km, 4-km domains only)
<b>Latent/Sensible Heat Flux</b>	Allowed
<b>Vertical Velocity Damping</b>	Switched off
<b>6th Order Horizontal Diffusion</b>	Simple (12-km domain only)

Table 2: Downslope windstorm events at KHIF as defined by this study.

Date	Time of max. wind, UTC	Max. wind speed $\text{m s}^{-1}$ (mph)	Max. wind gust $\text{m s}^{-1}$ (mph)
9 October 1979	1500	15 (34)	21 (48)
19 January 1980	1200	15 (34)	22 (49)
4 April 1983	1700	21 (46)	31 (70)
30 March 1984	1200	15 (34)	18 (41)
16 January 1987	1740	15 (34)	20 (44)
24 December 1987	0700	15 (34)	21 (46)
15 December 1988	1200	16 (36)	23 (51)
30 January 1993	1700	18 (41)	21 (48)
12 January 1997	1100	17 (38)	23 (52)
24 February 1997	1700	18 (40)	23 (51)
2 April 1997	1600	15 (34)	24 (53)
23 April 1999	1755	18 (40)	24 (53)
1 December 2011	1655	20 (45)	30 (67)

## 711 List of Figures

- 712 1 Terrain elevation and locations in northern Utah and western Wyoming (shad-  
713 ing). (a) Locations (Salt Lake International Airport, KSLC; and Hill Air Force  
714 Base, KHIF), mountain ranges, and cross-section paths mentioned in the text  
715 are shown. The shaded rectangular box along the Wasatch Front approxi-  
716 mately delineates the damage swath on 1 December 2011. The Wasatch Front  
717 is the low-lying region paralleling the west slopes of the Wasatch Mountains.  
718 (b) Zoomed-in view with locations discussed in the text. 36
- 719 2 Anemometers installed in Centerville, UT, by Union Pacific Railroad (MesoWest  
720 identifier: UP028; foreground) and Utah Department of Transportation (CEN;  
721 background), at the location of strongest observed winds during the 1 Decem-  
722 ber 2011 windstorm. 37
- 723 3 Domain areas for the 12-, 4-, and 1.3-km domains in the Weather Research  
724 and Forecasting model. Terrain is from the 12-km domain at 10-min resolution. 38
- 725 4 Sustained wind (shaded bars) associated with downslope windstorms as a  
726 function of winter season at KHIF according to the scale on left. Filled circles  
727 indicate the maximum gust associated with each windstorm. Percent of season  
728 with strong ( $10 \text{ m s}^{-1}$ ) 700-hPa winds from easterly direction in ERA-Interim  
729 Reanalysis data marked by black line according to scale on the right. Two  
730 (three) events occur in the winter of 1979/80 (1996/97) and hence overlap on  
731 the chart. 39
- 732 5 Evolution of ERA-Interim 700-hPa geopotential height (contoured at 30-m  
733 intervals), composited over 13 downslope windstorm events at (a) 0000 UTC,  
734 (b) 0600 UTC, (c) 1200 UTC, and (d) 1800 UTC. 40

- 735 6 Evolution of 700-hPa geopotential height (contoured at 30-m intervals) and  
736 wind speed (shading according to scale) on 1 December 2011, taken from the  
737 ERA-Interim dataset, at (a) 0000 UTC, (b) 0600 UTC, (c) 1200 UTC, and  
738 (d) 1800 UTC. 41
- 739 7 Mobile wind observations from 0915–1015 UTC. Vector arrows are relative to  
740 scale in top-left. Distance is according to the scale in bottom-left. Filled  
741 contours indicate terrain, taken from innermost WRF domain, with scale at  
742 bottom. Observation stations mentioned in text are labeled. 42
- 743 8 Surface wind observations at (a) KHIF, (b) UFD04, and (c) OGP on 1 De-  
744 cember 2011. Wind speed, wind gust, and wind direction shown by solid  
745 lines, filled circles, and crosses, respectively. All available KHIF observations  
746 are shown; for clarity, UFD04 and OGP data are sampled at 30-min intervals  
747 from the data available at higher reporting intervals. 43
- 748 9 Skew-T log-P profiles at 1200 UTC 1 December 2011, from observed rawin-  
749 sonde launch at KSLC (black lines) and from the WRF Control simulation  
750 at the nearest grid point (blue lines). Temperature, dew-point temperature,  
751 and wind denoted by solid lines, dashed lines, and barbs (full barb  $5 \text{ m s}^{-1}$ ),  
752 respectively. For clarity, wind barbs from only selected model levels are shown. 44
- 753 10 Vertical profiles of observed rawinsonde data near Morgan, UT, and Cen-  
754 terville, UT (near UP028). (a) Potential temperature (solid line), relative  
755 humidity (dashed line), wind speed (crosses), and wind direction (open cir-  
756 cles) at Morgan, UT, at 1800 UTC 1 December 2011, as a function of height.  
757 (b) As in (a) but for the 1200 UTC Centerville, UT launch. 45
- 758 11 Comparison of rawinsonde ascent rates ( $\text{m s}^{-1}$ ) at Morgan, UT (1800 UTC;  
759 crosses) and Centerville (1200 UTC; open circles). 46

- 760 12 WRF Control simulation 700-hPa geopotential height fields (contoured at 30-  
761 m interval), at (a) 0000 UTC, (b) 0600 UTC, (c) 1200 UTC, and (d) 1800  
762 UTC, all 1 December 2011. Noisy contours result from the 700-hPa surface  
763 intersecting the model terrain. 47
- 764 13 Comparison of observed surface wind speeds (colored circles) versus Control-  
765 simulation surface wind speeds (shading), both according to scale at bottom.  
766 The wind measurements are taken from the observation time closest to (a)  
767 1200 UTC and (b) 2100 UTC, within 30 min either side of the respective times,  
768 for each available station. WRF innermost-domain terrain contoured every  
769 400 m for reference; Antelope Island marked with “AI”. 48
- 770 14 Observed and simulated surface winds at Farmington (UFD04), UT on 1  
771 December 2011. Observed wind speeds and wind directions from UFD04 are  
772 denoted by black solid lines and filled circles, respectively. Simulated surface  
773 wind speeds and directions from the Control (No-Uinta) simulations are shown  
774 by the green (red) solid lines and filled circles, respectively. Wind direction  
775 data from all three sources have been subsampled to every 20 minutes for clarity. 49
- 776 15 Perpendicular-to-Wasatch cross-section from innermost WRF domain (A–B in  
777 Fig. 1) at (a) 1200 UTC and (b) 2100 UTC, 1 December 2011. Shading denotes  
778 plane-parallel wind component according to the scale (e.g., blue indicates flow  
779 from right to left), while potential temperature is contoured at an interval of  
780 2 K. 50
- 781 16 Roughly north–south cross-section from innermost WRF domain (C–D in  
782 Fig. 1) through west-central Wyoming (left) to the southern slopes of the  
783 Uintas (right) at (a) 1200 UTC and (b) 2100 UTC, 1 December 2011. Shad-  
784 ing denotes wind component in and out of the page (e.g., blue indicates pre-  
785 dominantly easterly flow out of the page) according to the scale; potential  
786 temperature is contoured at an interval of 2 K. 51

- 787 17 Zonal wind difference (No Uinta minus Control), shaded according to the scale  
788 at the bottom, at (a) 1200 UTC and (b) 2100 UTC, 1 December 2011. Black  
789 (red) contours at 500-m intervals denote the elevation of the terrain used  
790 in both the Control and No Uinta (Control only) simulations. Blue (red)  
791 indicates an increase (decrease) in easterly wind in this location as a result of  
792 removing the Uinta mountains. 52
- 793 18 As in Fig. 15, but from the no Uinta WRF simulation. 53
- 794 19 As in Fig. 16, but from the no Uinta WRF simulation. 54

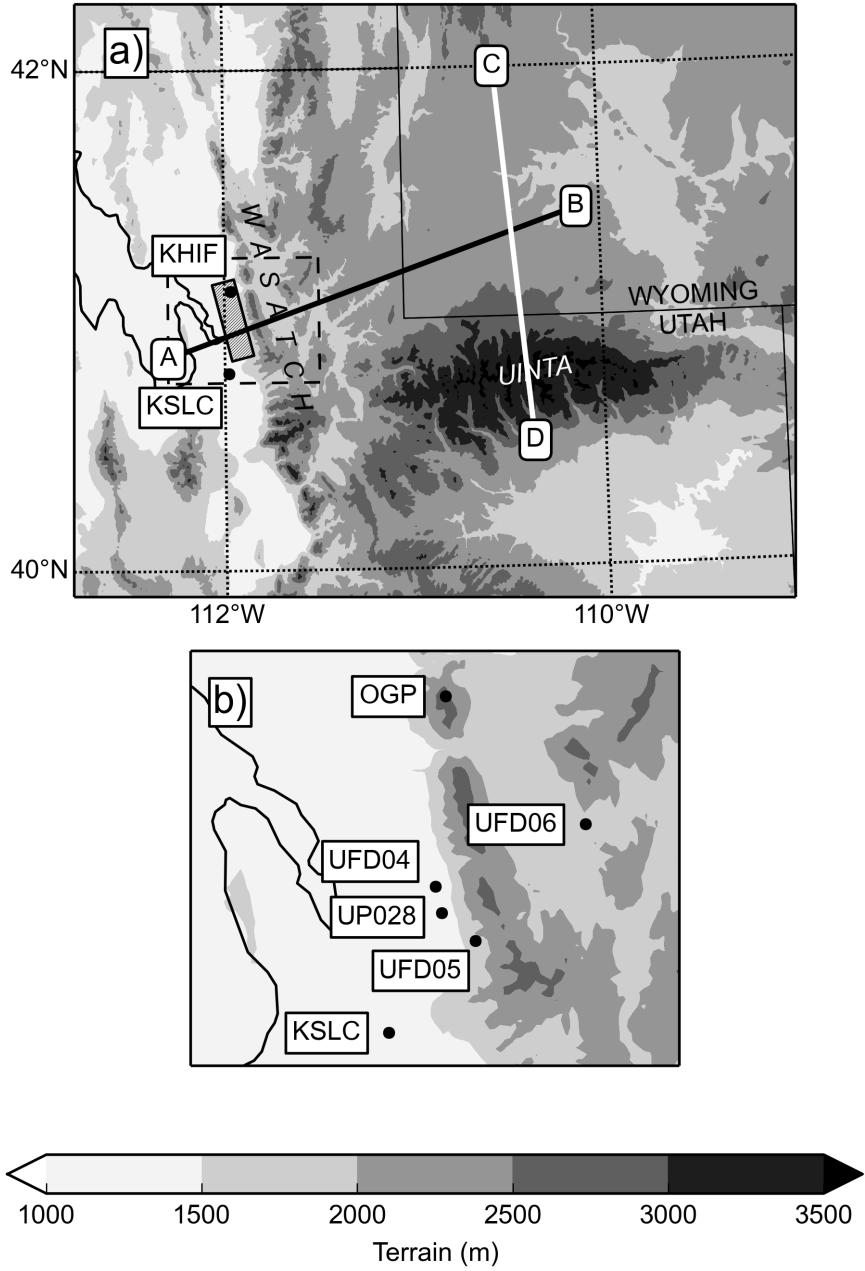


Figure 1: Terrain elevation and locations in northern Utah and western Wyoming (shading). (a) Locations (Salt Lake International Airport, KSLC; and Hill Air Force Base, KHIF), mountain ranges, and cross-section paths mentioned in the text are shown. The shaded rectangular box along the Wasatch Front approximately delineates the damage swath on 1 December 2011. The Wasatch Front is the low-lying region paralleling the west slopes of the Wasatch Mountains. (b) Zoomed-in view with locations discussed in the text.



Figure 2: Anemometers installed in Centerville, UT, by Union Pacific Railroad (MesoWest identifier: UP028; foreground) and Utah Department of Transportation (CEN; background), at the location of strongest observed winds during the 1 December 2011 windstorm.

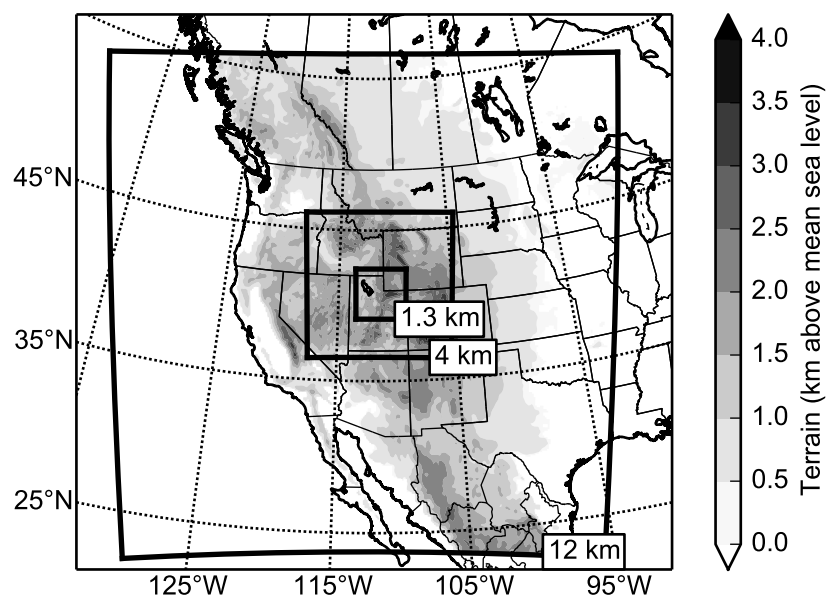


Figure 3: Domain areas for the 12-, 4-, and 1.3-km domains in the Weather Research and Forecasting model. Terrain is from the 12-km domain at 10-min resolution.

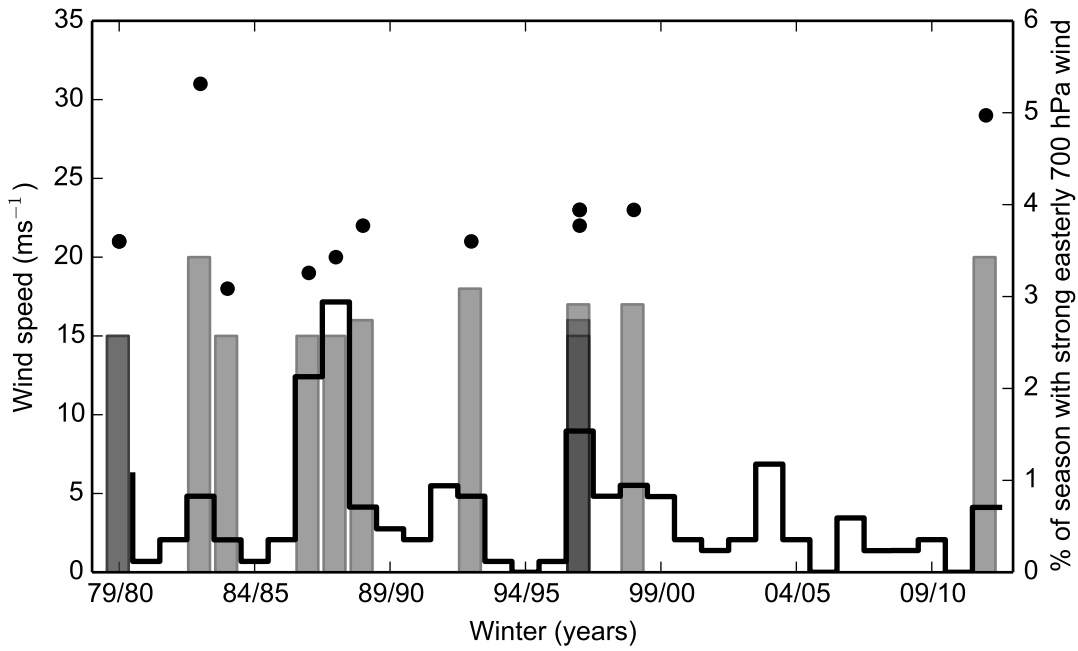


Figure 4: Sustained wind (shaded bars) associated with downslope windstorms as a function of winter season at KHIF according to the scale on left. Filled circles indicate the maximum gust associated with each windstorm. Percent of season with strong ( $10 \text{ m s}^{-1}$ ) 700-hPa winds from easterly direction in ERA-Interim Reanalysis data marked by black line according to scale on the right. Two (three) events occur in the winter of 1979/80 (1996/97) and hence overlap on the chart.

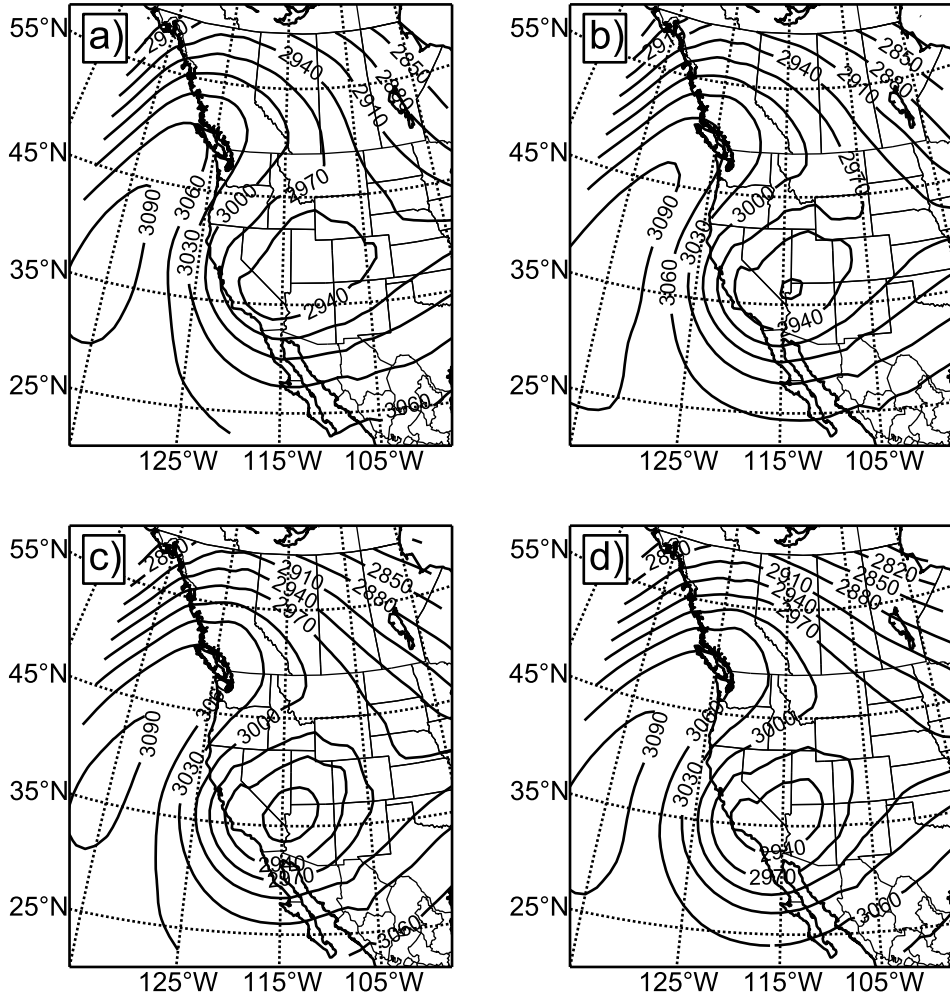


Figure 5: Evolution of ERA-Interim 700-hPa geopotential height (contoured at 30-m intervals), composited over 13 downslope windstorm events at (a) 0000 UTC, (b) 0600 UTC, (c) 1200 UTC, and (d) 1800 UTC.

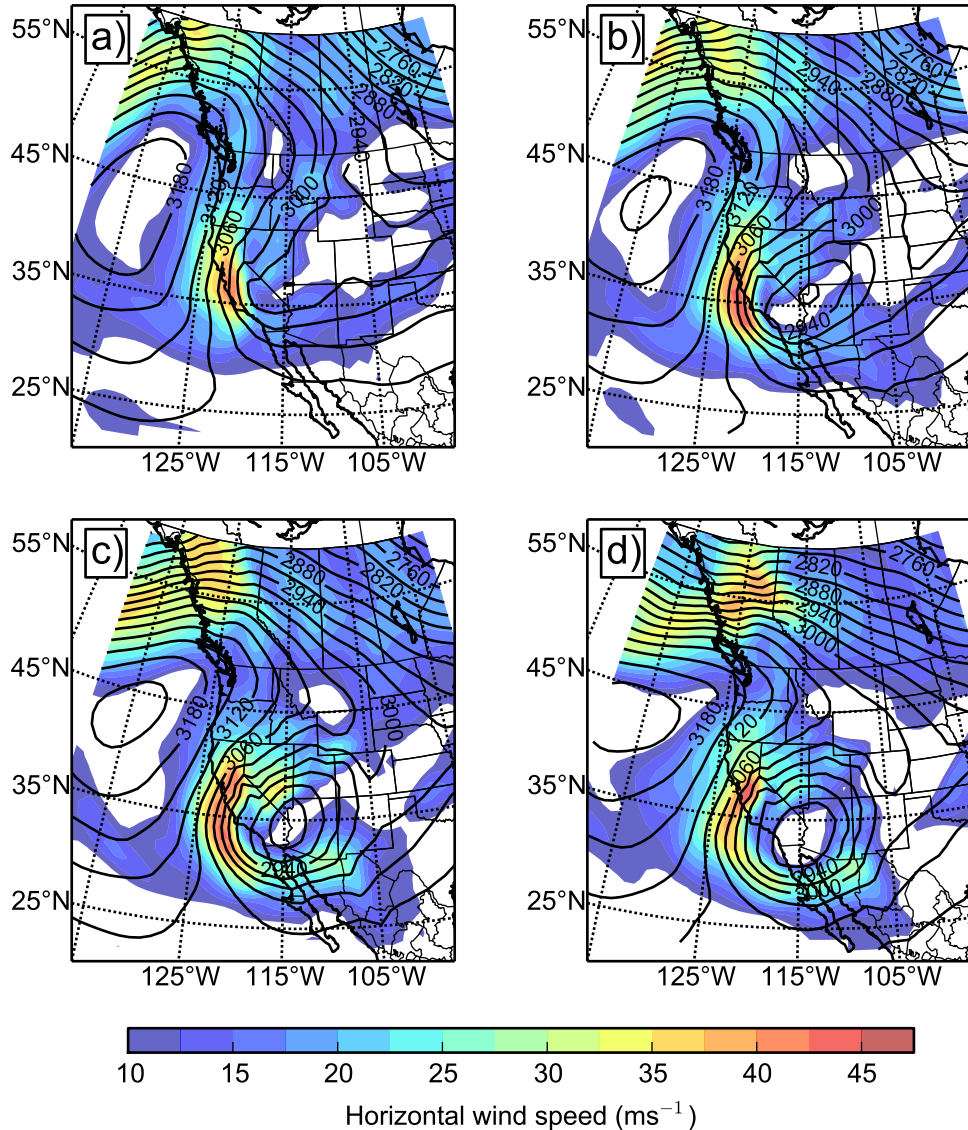


Figure 6: Evolution of 700-hPa geopotential height (contoured at 30-m intervals) and wind speed (shading according to scale) on 1 December 2011, taken from the ERA-Interim dataset, at (a) 0000 UTC, (b) 0600 UTC, (c) 1200 UTC, and (d) 1800 UTC.

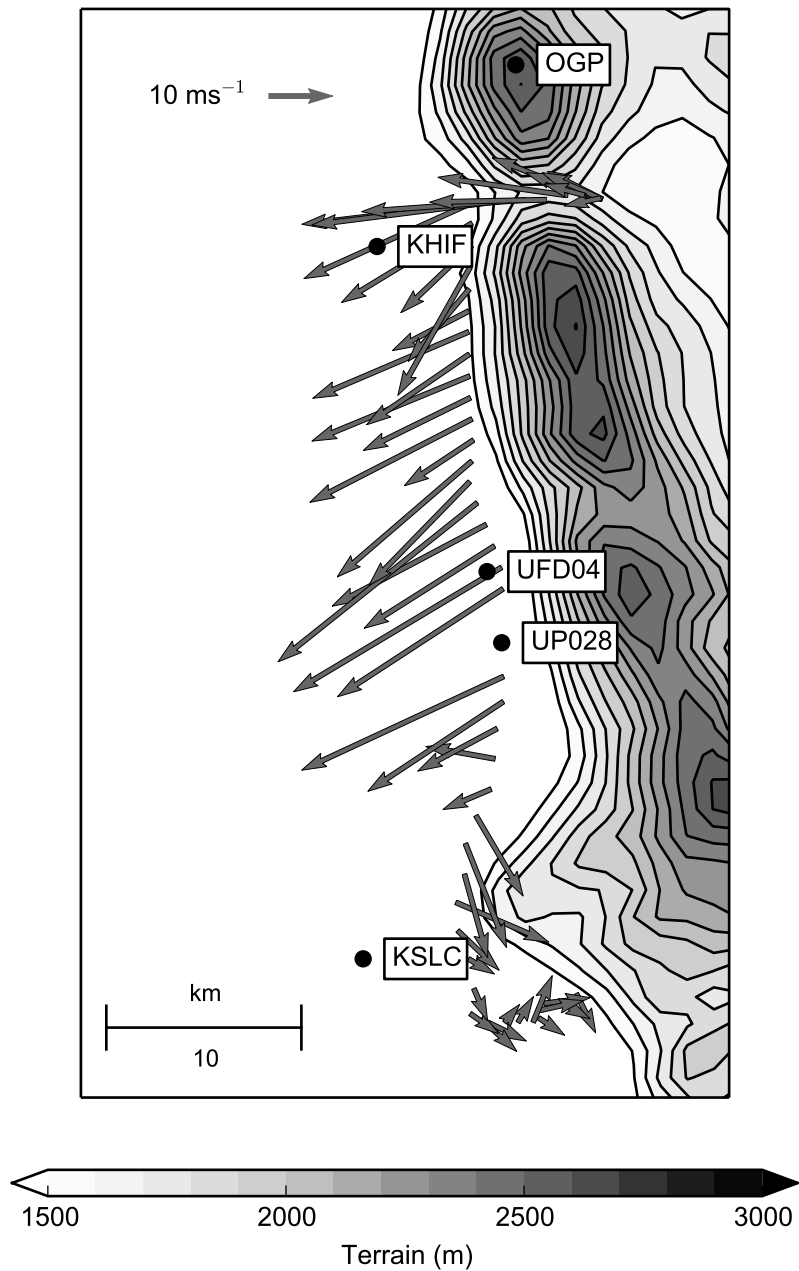


Figure 7: Mobile wind observations from 0915–1015 UTC. Vector arrows are relative to scale in top-left. Distance is according to the scale in bottom-left. Filled contours indicate terrain, taken from innermost WRF domain, with scale at bottom. Observation stations mentioned in text are labeled.

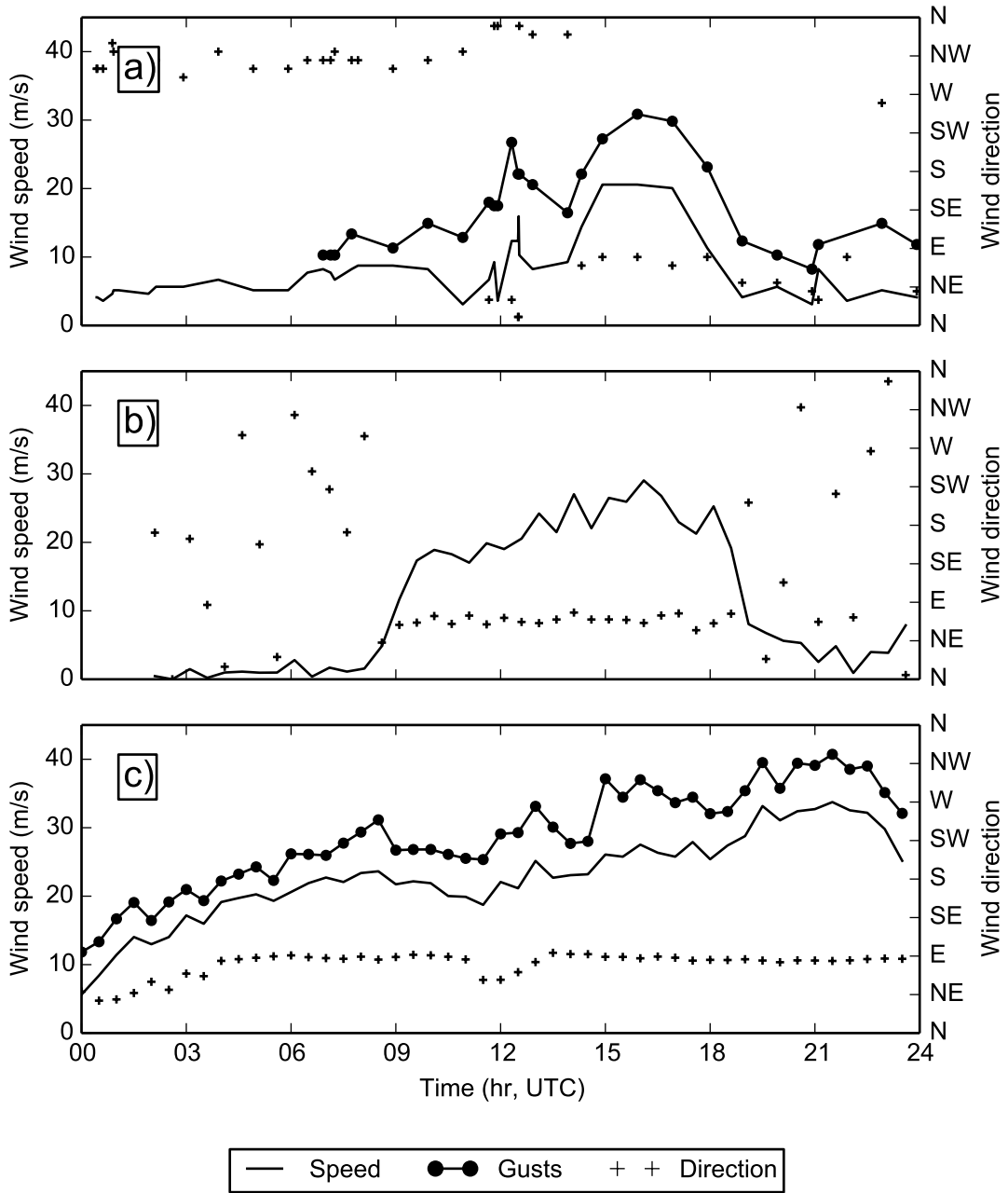


Figure 8: Surface wind observations at (a) KHIF, (b) UFD04, and (c) OGP on 1 December 2011. Wind speed, wind gust, and wind direction shown by solid lines, filled circles, and crosses, respectively. All available KHIF observations are shown; for clarity, UFD04 and OGP data are sampled at 30-min intervals from the data available at higher reporting intervals.

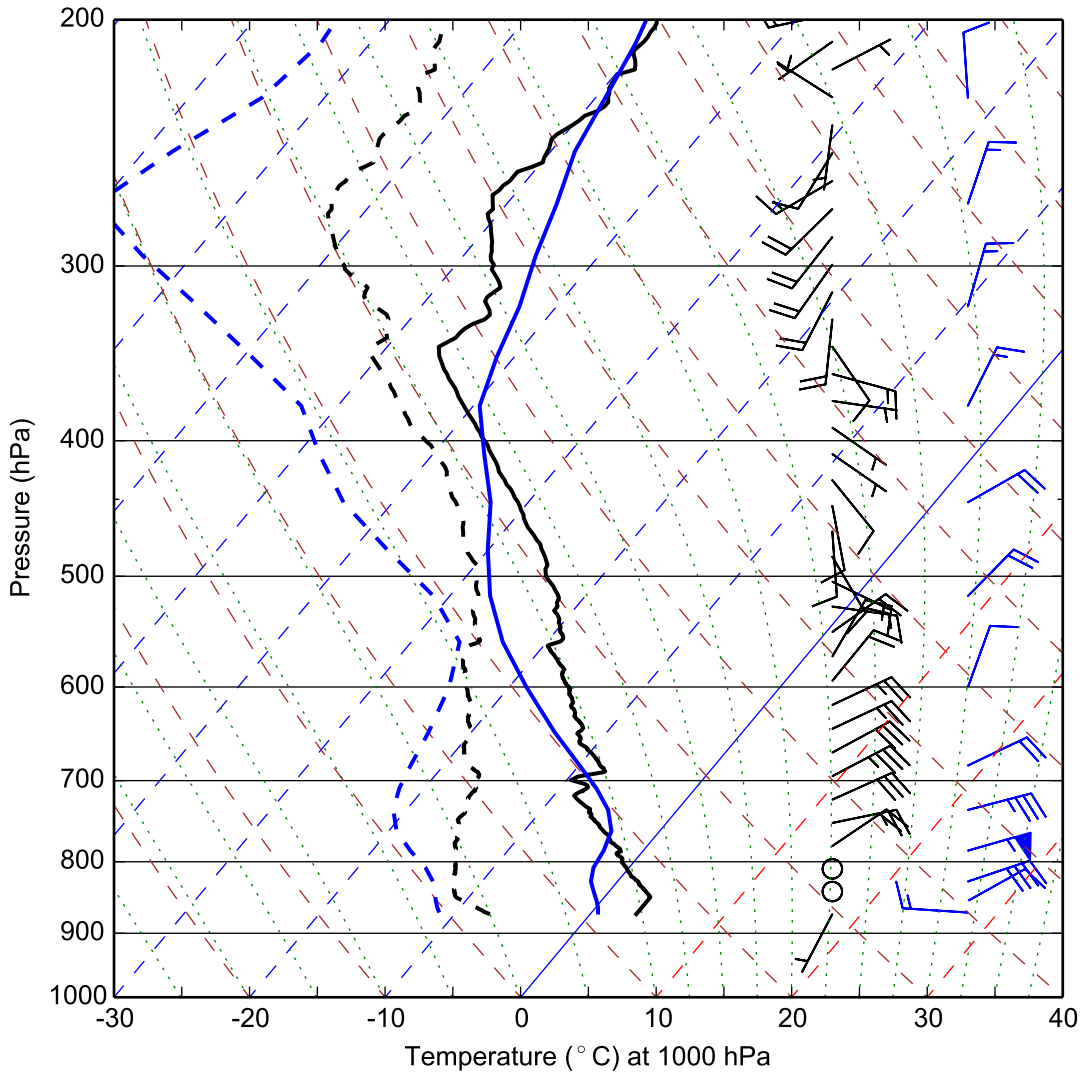
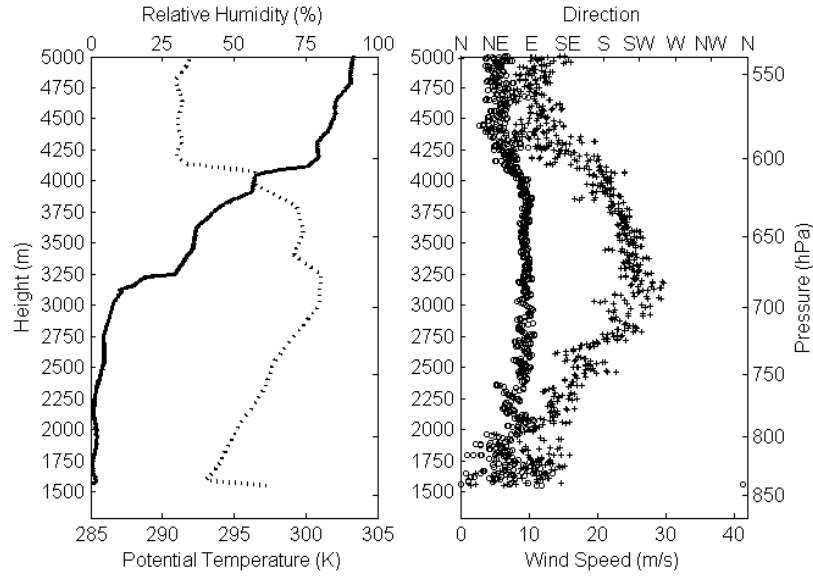
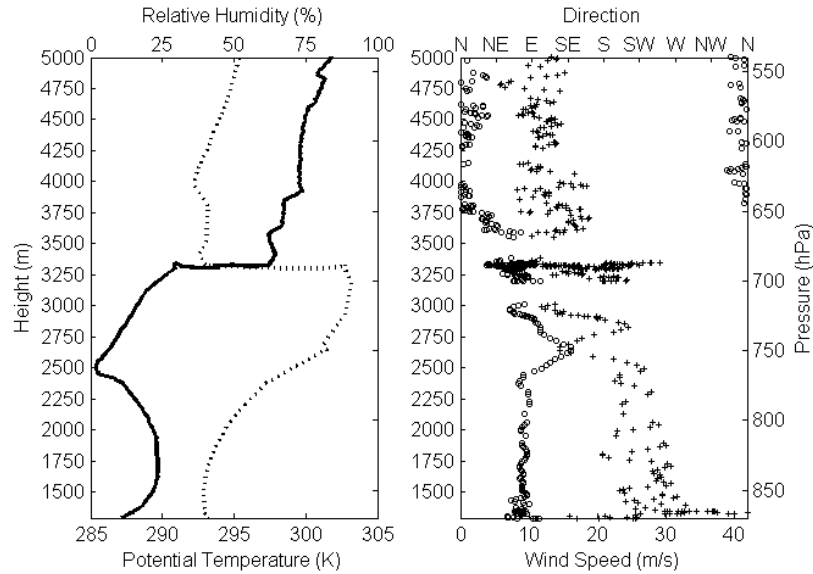


Figure 9: Skew-T log-P profiles at 1200 UTC 1 December 2011, from observed rawinsonde launch at KSLC (black lines) and from the WRF Control simulation at the nearest grid point (blue lines). Temperature, dew-point temperature, and wind denoted by solid lines, dashed lines, and barbs (full barb  $5 \text{ m s}^{-1}$ ), respectively. For clarity, wind barbs from only selected model levels are shown.



**(a) Morgan (UFD06)**



**(b) Centerville**

Figure 10: Vertical profiles of observed rawinsonde data near Morgan, UT, and Centerville, UT (near UP028). (a) Potential temperature (solid line), relative humidity (dashed line), wind speed (crosses), and wind direction (open circles) at Morgan, UT, at 1800 UTC 1 December 2011, as a function of height. (b) As in (a) but for the 1200 UTC Centerville, UT launch.

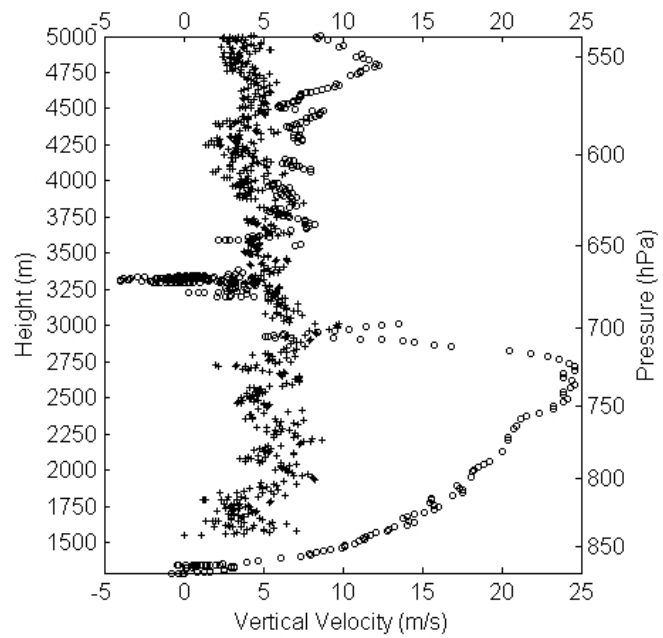


Figure 11: Comparison of rawinsonde ascent rates ( $\text{m s}^{-1}$ ) at Morgan, UT (1800 UTC; crosses) and Centerville (1200 UTC; open circles).

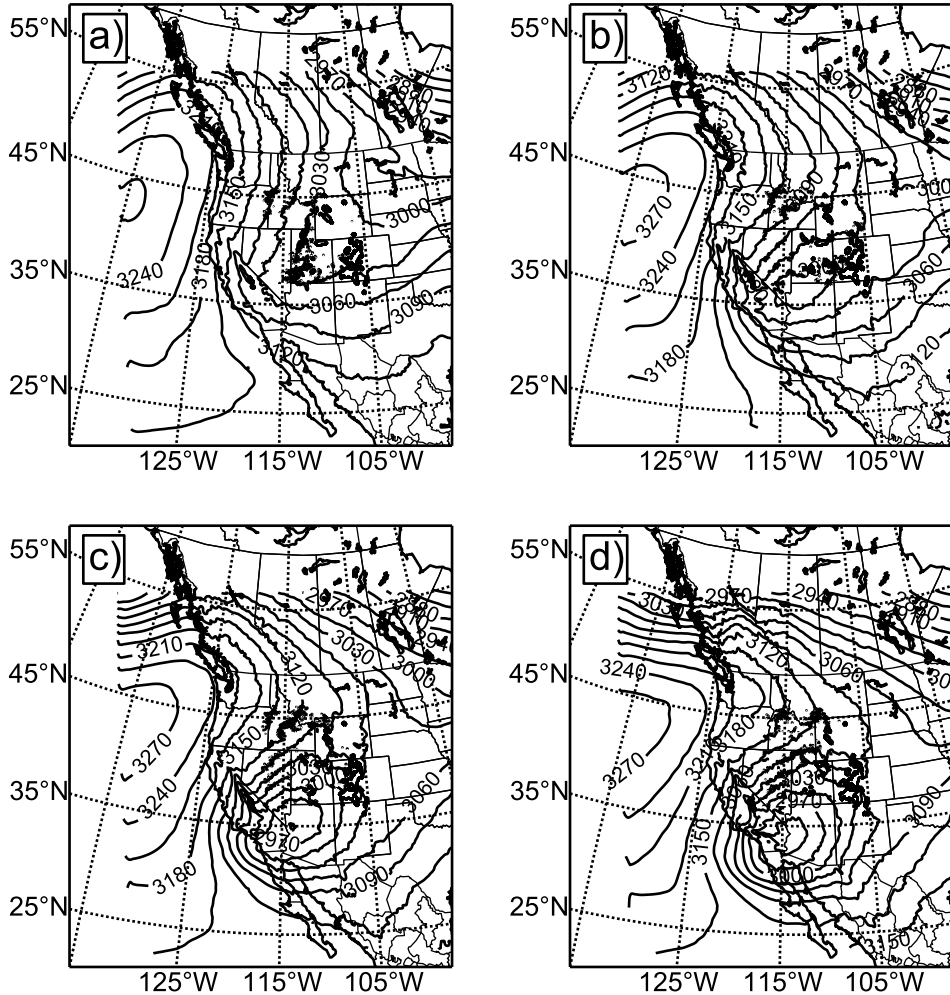


Figure 12: WRF Control simulation 700-hPa geopotential height fields (contoured at 30-m interval), at (a) 0000 UTC, (b) 0600 UTC, (c) 1200 UTC, and (d) 1800 UTC, all 1 December 2011. Noisy contours result from the 700-hPa surface intersecting the model terrain.

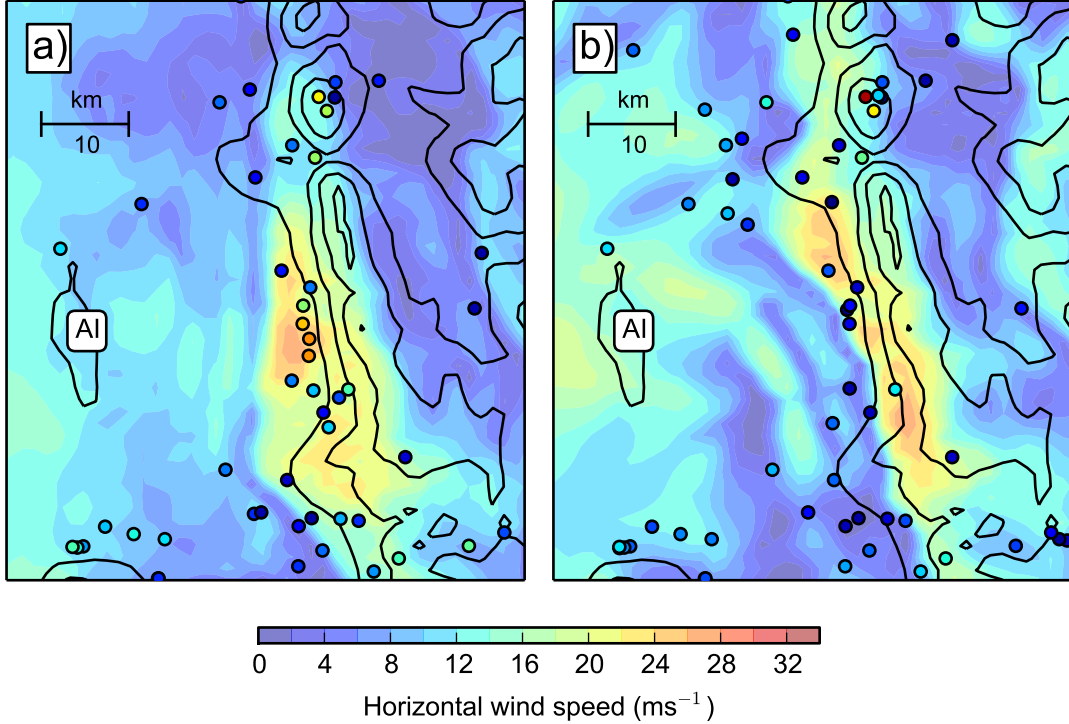


Figure 13: Comparison of observed surface wind speeds (colored circles) versus Control-simulation surface wind speeds (shading), both according to scale at bottom. The wind measurements are taken from the observation time closest to (a) 1200 UTC and (b) 2100 UTC, within 30 min either side of the respective times, for each available station. WRF innermost-domain terrain contoured every 400 m for reference; Antelope Island marked with “AI”.

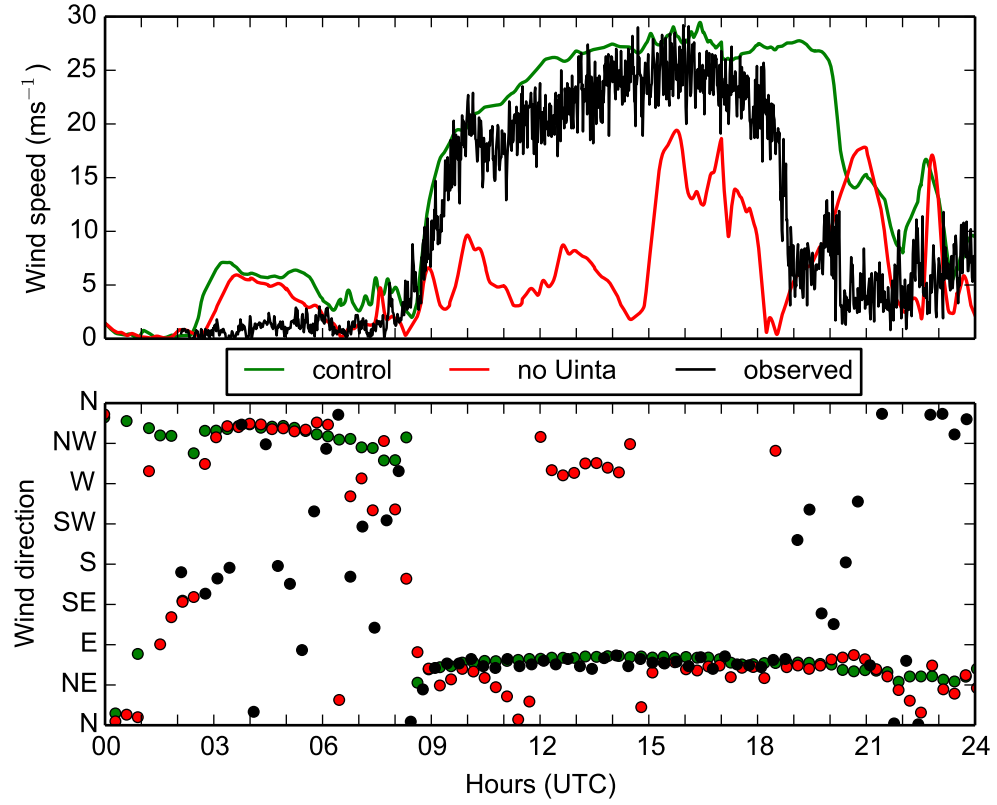


Figure 14: Observed and simulated surface winds at Farmington (UFD04), UT on 1 December 2011. Observed wind speeds and wind directions from UFD04 are denoted by black solid lines and filled circles, respectively. Simulated surface wind speeds and directions from the Control (No Uinta) simulations are shown by the green (red) solid lines and filled circles, respectively. Wind direction data from all three sources have been subsampled to every 20 minutes for clarity.

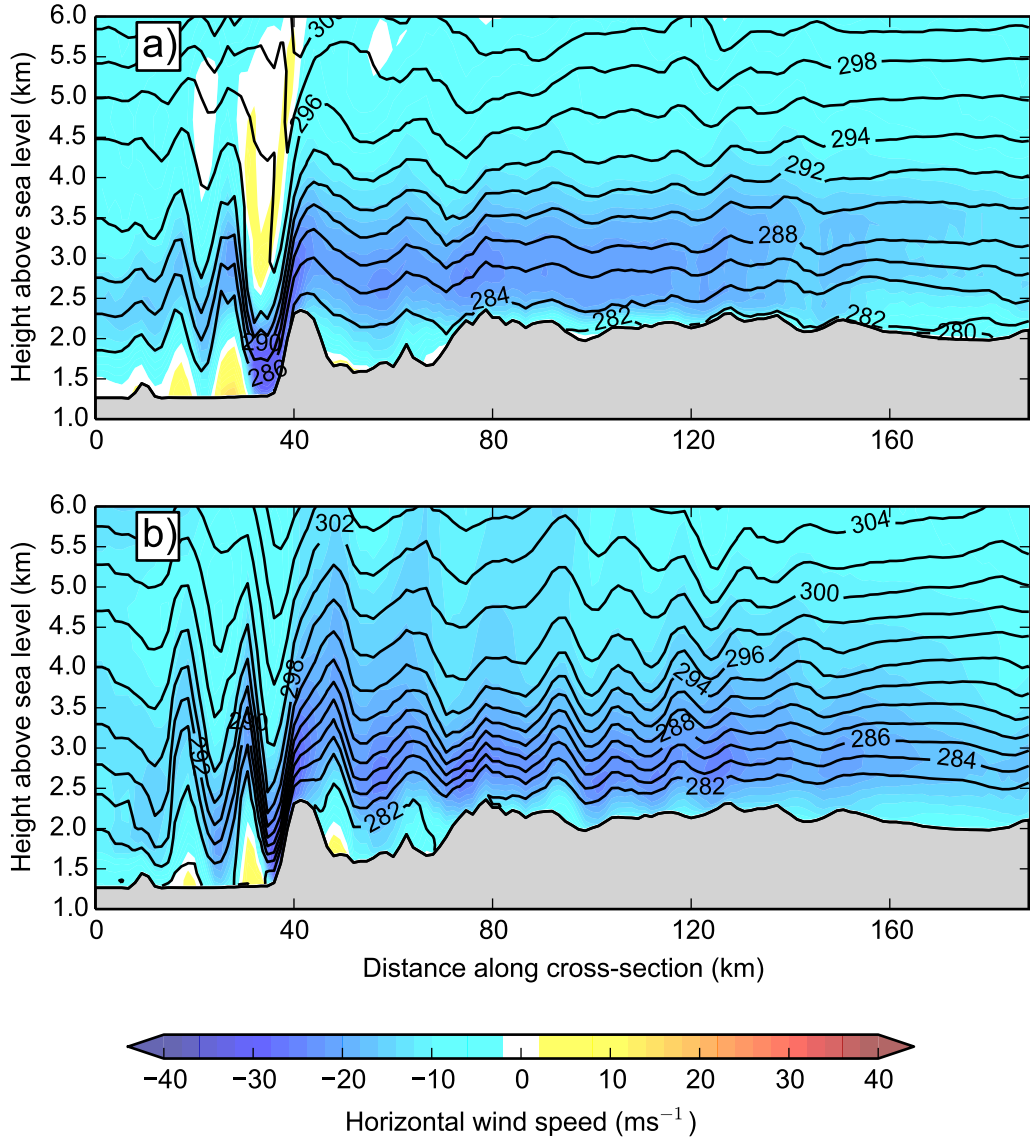


Figure 15: Perpendicular-to-Wasatch cross-section from innermost WRF domain (A–B in Fig. 1) at (a) 1200 UTC and (b) 2100 UTC, 1 December 2011. Shading denotes plane-parallel wind component according to the scale (e.g., blue indicates flow from right to left), while potential temperature is contoured at an interval of 2 K.

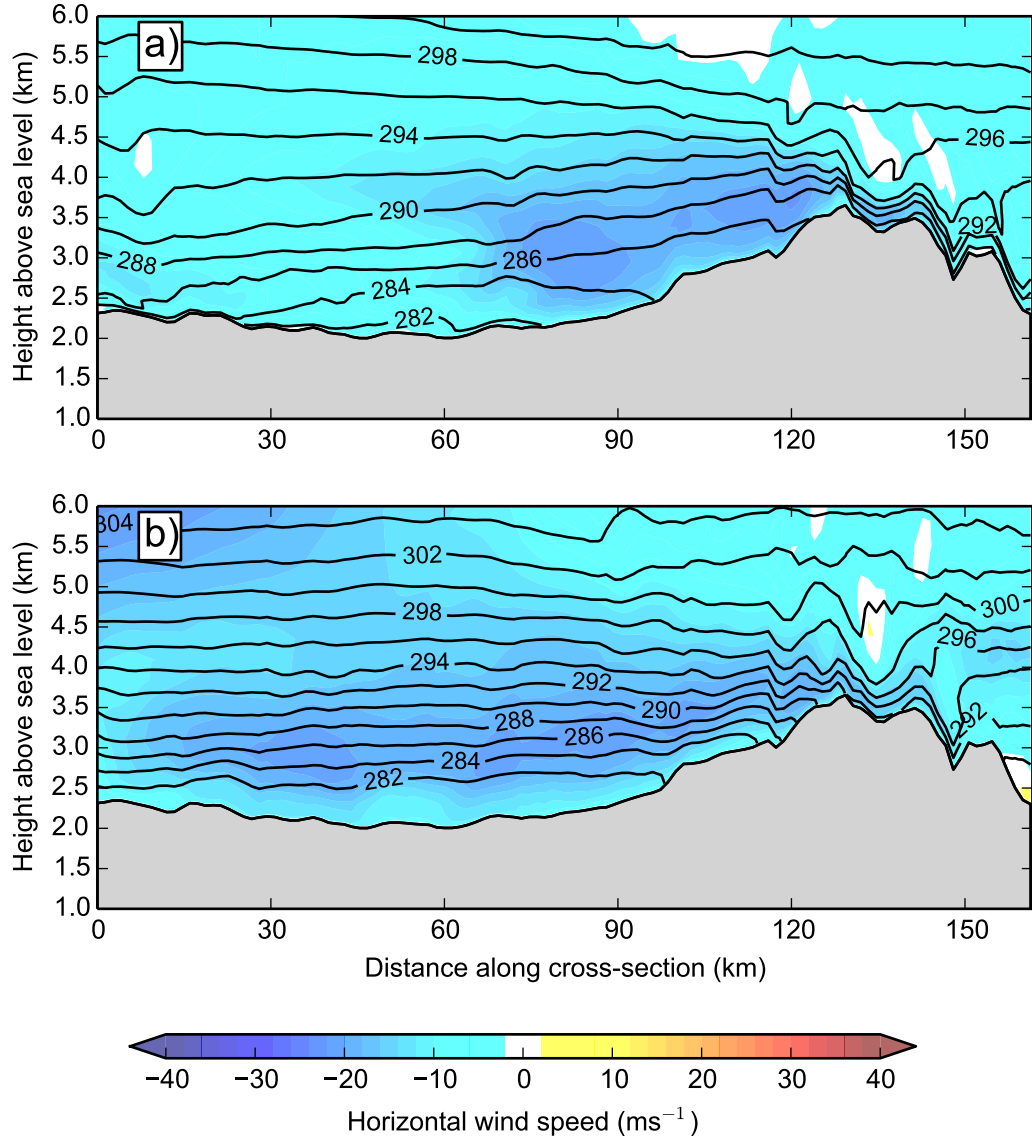


Figure 16: Roughly north–south cross-section from innermost WRF domain (C–D in Fig. 1) through west-central Wyoming (left) to the southern slopes of the Uintas (right) at (a) 1200 UTC and (b) 2100 UTC, 1 December 2011. Shading denotes wind component in and out of the page (e.g., blue indicates predominantly easterly flow out of the page) according to the scale; potential temperature is contoured at an interval of 2 K.

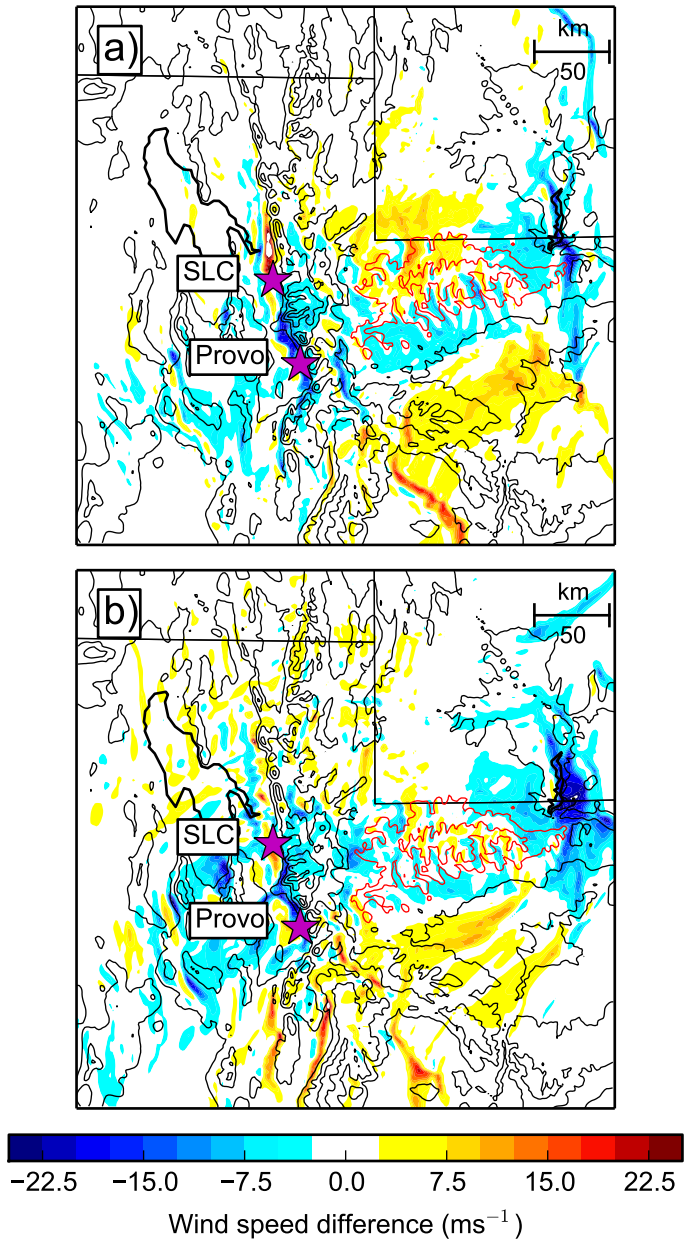


Figure 17: Zonal wind difference (No-Uinta minus Control), shaded according to the scale at the bottom, at (a) 1200 UTC and (b) 2100 UTC, 1 December 2011. Black (red) contours at 500-m intervals denote the elevation of the terrain used in both the Control and No-Uinta (Control only) simulations. Blue (red) indicates an increase (decrease) in easterly wind in this location as a result of removing the Uinta mountains.

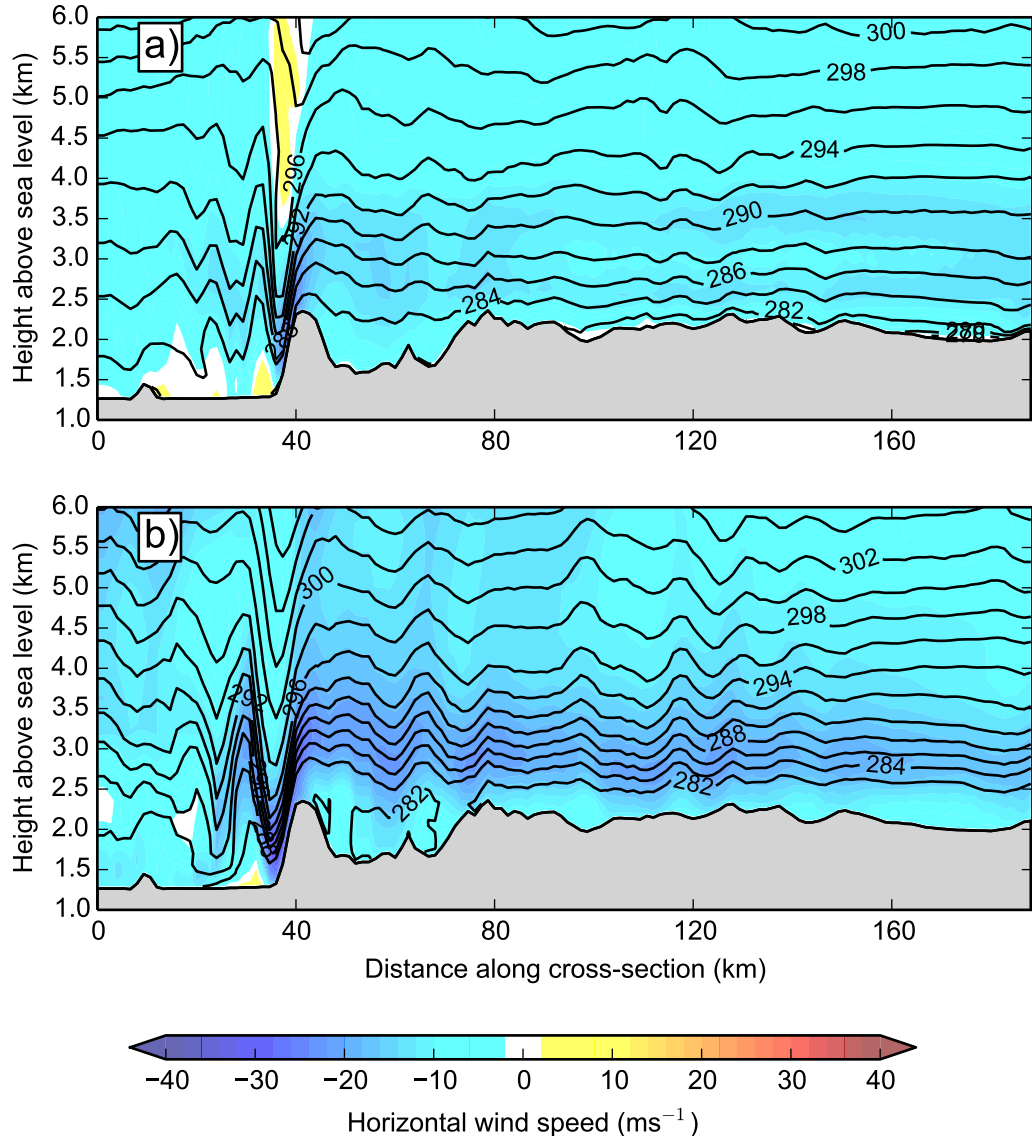


Figure 18: As in Fig. 15, but from the no-Uinta WRF simulation.

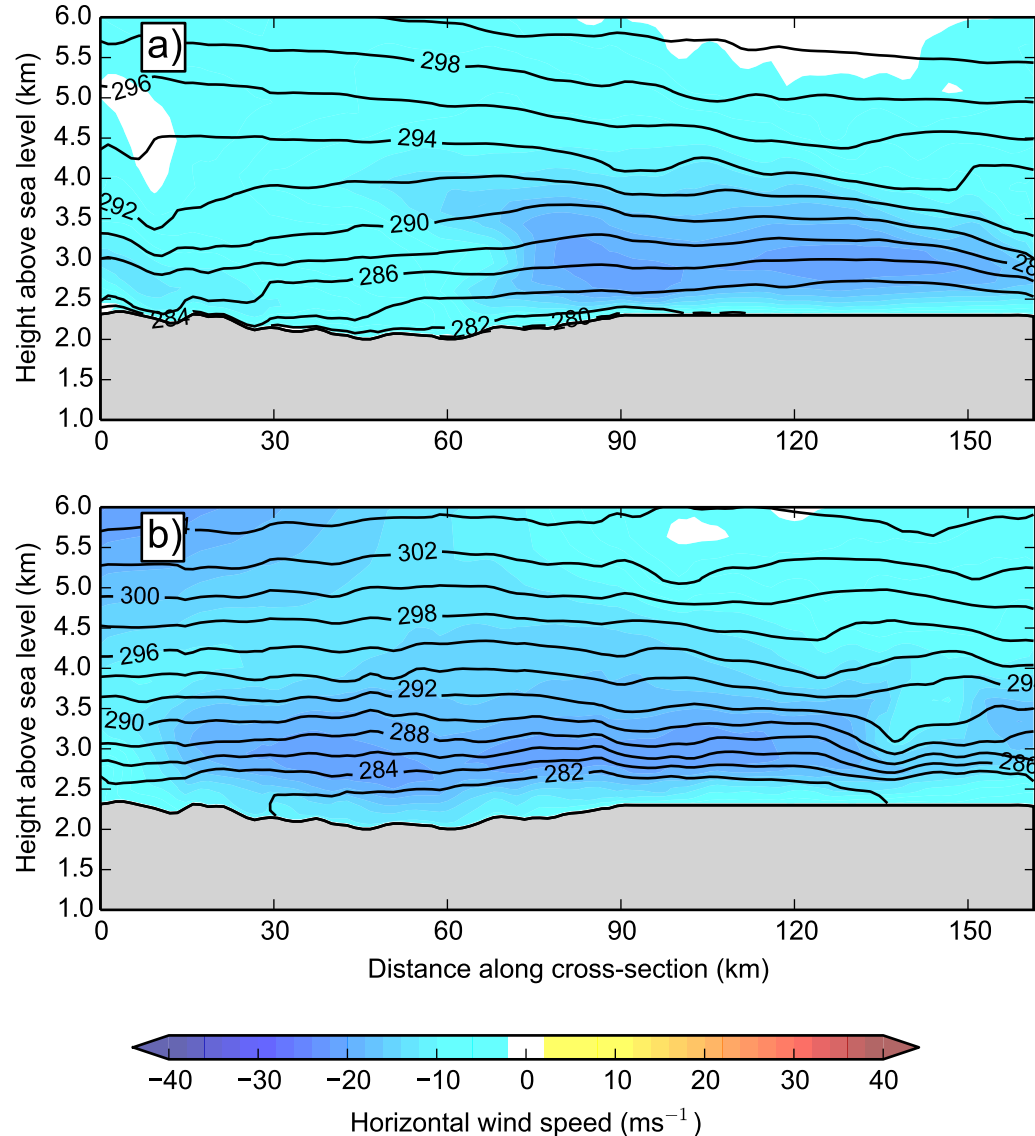


Figure 19: As in Fig. 16, but from the no-Uinta WRF simulation.